

Nano Active Stabilization System - Uniaxial Model

Dehaeze Thomas

April 2, 2024

Contents

1	Micro Station Model	6
1.1	Measured dynamics	7
1.2	Uniaxial Model	7
1.3	Comparison of the model and measurements	8
2	Nano-Hexapod Model	9
2.1	Nano-Hexapod Parameters	10
2.2	Obtained Dynamic Response	10
3	Disturbance Identification	12
3.1	Ground Motion	13
3.2	Stage Vibration	13
4	Open-Loop Dynamic Noise Budgeting	16
4.1	Sensitivity to disturbances	16
4.2	Open-Loop Dynamic Noise Budgeting	16
5	Active Damping	19
5.1	Active Damping Strategies	20
5.2	Plant Dynamics for Active Damping	21
5.3	Achievable Damping - Root Locus	22
5.4	Change of sensitivity to disturbances	23
5.5	Noise Budgeting after Active Damping	24
5.6	Obtained Closed Loop Response	24
5.7	Robustness to change of payload's mass	27
6	Position Feedback Controller	28
6.1	Damped Plant Dynamics	29
6.2	Position Feedback Controller	29
6.3	Closed-Loop Noise Budgeting	31
7	Effect of limited micro-station compliance	34
7.1	Neglected support compliance	34
7.2	Effect of support compliance on L/F	35
7.3	Effect of support compliance on d/F	35
8	Effect of Payload Dynamics	38
8.1	Impact on the plant dynamics	38
8.2	Impact on the positioning stability	41
9	Conclusion	44
	Bibliography	45

In this report, a uniaxial model of the Nano Active Stabilization System (NASS) is developed and used to have a first idea of the challenges involved in this complex system. Note that in this document, only the vertical direction is considered (which is the most stiff), but other directions were considered as well and yields similar conclusions. The model is schematically shown in Figure 1 where the colors are representing the studied parts in different sections.

In order to have a relevant model, the micro-station dynamics is first identified and its model is tuned to match the measurements (Section 1). Then, a model of the nano-hexapod is added on top of the micro-station. With added sample and sensors, this gives a uniaxial dynamical model of the NASS that will be used for further analysis (Section 2).

The disturbances affecting the position stability are identified experimentally (Section 3) and included in the model for dynamical noise budgeting (Section 4). In all the following analysis, there nano-hexapod stiffnesses are considered to better understand the trade-offs and to find the most adequate nano-hexapod design. Three sample masses are also considered to verify the robustness of the applied control strategies to a change of sample.

Three active damping techniques are then applied on the nano-hexapod. This helps to reduce the effect of disturbances as well as render the system easier to control afterwards (Section 5).

Once the system is well damped, a feedback position controller is applied, and the obtained performance are compared (Section 6).

Two key effects that may limit that positioning performances are then considered: the limited micro-station compliance (Section 7) and the presence of dynamics between the nano-hexapod and the sample's point of interest (Section 8).

Conclusion remarks are given in Section 9.

Table 1: Report sections and corresponding Matlab files

Sections	Matlab File
Section 1	uniaxial_1_micro_station_model.m
Section 2	uniaxial_2_nano_hexapod_model.m
Section 3	uniaxial_3_disturbances.m
Section 4	uniaxial_4_dynamic_noise_budget.m
Section 5	uniaxial_5_active_damping.m
Section 6	uniaxial_6_hac_lac.m
Section 7	uniaxial_7_support_compliance
Section 8	uniaxial_8_payload_dynamics

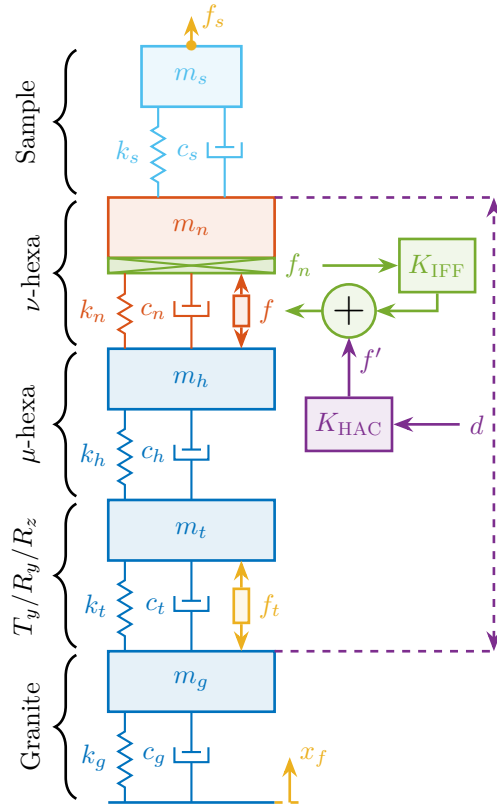


Figure 1: Uniaxial Micro-Station model in blue (Section 1), Nano-Hexapod models in red (Section 2), Disturbances in yellow (Section 3), Active Damping in green (Section 5), Position control in purple (Section 6) and Sample dynamics in cyan (Section 8)

1 Micro Station Model

In this section, a uni-axial model of the micro-station is tuned in order to match measurements made on the micro-station. The measurement setup is shown in Figure 1.1 where several geophones are fixed to the micro-station and an instrumented hammer is used to inject forces on different stages of the micro-station.

From the measured frequency response functions (FRF), the model can be tuned to approximate the uniaxial dynamics of the micro-station.

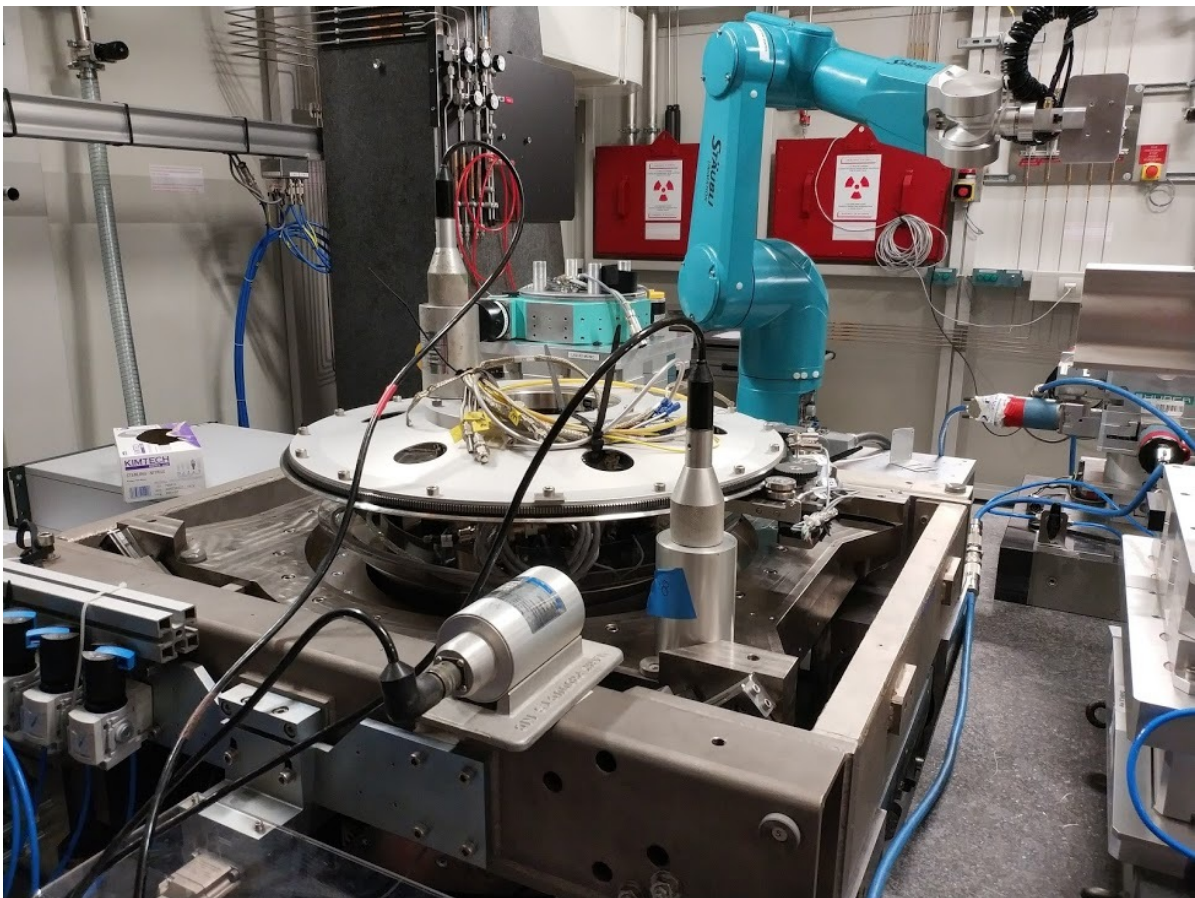


Figure 1.1: Experimental Setup for the first dynamical measurements on the Micro-Station. Geophones are fixed to the micro-station, and the granite as well as the micro-hexapod's top platform are impact with an instrumented hammer

1.1 Measured dynamics

The measurement setup is schematically shown in Figure 1.2a where:

- Two hammer hits are performed, one on the Granite (force F_g), and one on the micro-hexapod's top platform (force F_h)
- The inertial motion of the granite x_g and the micro-hexapod's top platform x_h are measured using geophones.

From the forces applied by the instrumented hammer and the responses of the geophones, the following frequency response functions can be computed:

- from F_h to d_h (i.e. the compliance of the micro-station)
- from F_g to d_h (or from F_h to d_g)
- from F_g to d_g

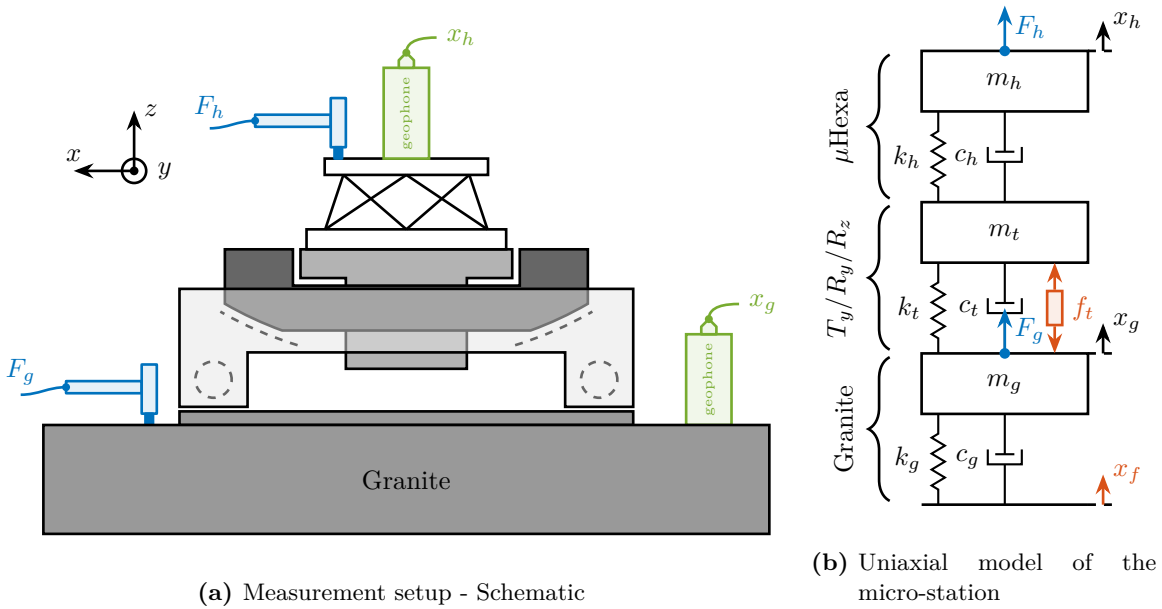


Figure 1.2: Schematic of the Micro-Station measurement setup and uniaxial model.

Due to the bad coherence at low frequency, the frequency response functions will only be shown between 20 and 200Hz (solid lines in Figure 1.3).

1.2 Uniaxial Model

The uni-axial model of the micro-station is shown in Figure 1.2b, with:

- Disturbances:

- x_f : Floor motion
- f_t : Stage vibrations
- Hammer impacts: F_h and F_g .
- Geophones: x_h and x_g

Masses are estimated from the CAD. And stiffnesses from the data-sheet of stage manufacturers. The damping coefficients are tuned to match the identified damping from the measurements.

1.3 Comparison of the model and measurements

The comparison between the measurements and the model is shown in Figure 1.3.

Only three modes are modelled with frequencies at 70Hz, 140Hz and 320Hz.

As the model is simplistic, the goal is not to match exactly the measurement but to have a first approximation. More accurate models will be used later on.

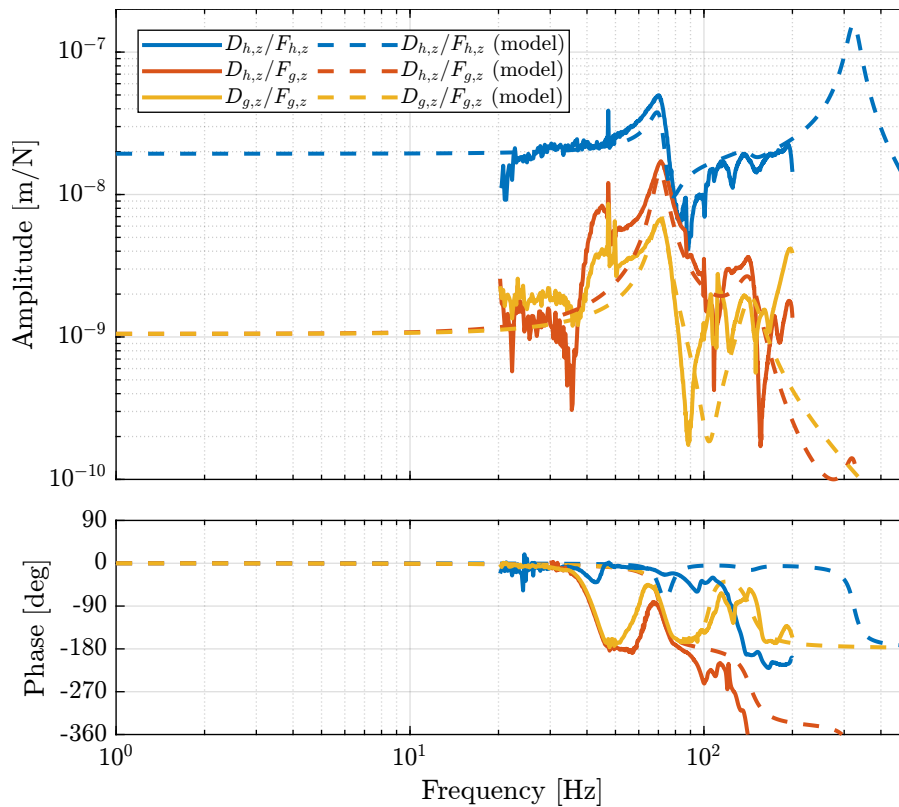


Figure 1.3: Comparison of the measured FRF and identified ones from the uni-axial model

2 Nano-Hexapod Model

A model of the nano-hexapod and sample is now added on top of the uni-axial model of the micro-station (Figure 2.1).

Disturbances (shown in red) are:

- f_s : direct forces applied to the sample (for instance cable forces)
- f_t : disturbances coming from the imperfect stage scanning performance
- x_f : floor motion

The control signal is the force applied by the nano-hexapod f and the measurement is the relative motion between the sample and the granite d .

The sample is here considered as a rigid body and rigidly fixed to the nano-hexapod. The effect of having resonances between the sample's point of interest and the nano-hexapod actuator will be considered in further analysis.

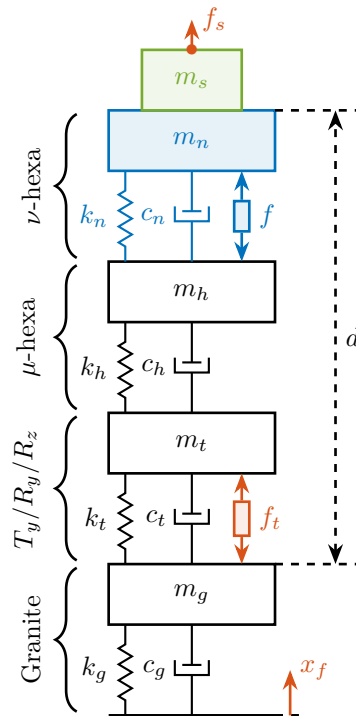


Figure 2.1: Uni-axial model of the micro-station with added nano-hexapod (represented in blue) and sample (represented in green)

2.1 Nano-Hexapod Parameters

The parameters for the nano-hexapod and sample are:

- m_s the sample mass that can vary from 1kg up to 50kg
- m_n the nano-hexapod mass which is set to 15kg
- k_n the nano-hexapod stiffness, which can vary depending on the chosen architecture/technology

As a first example, let's choose a nano-hexapod stiffness of $10\text{ N}/\mu\text{m}$ and a sample mass of 10kg.

2.2 Obtained Dynamic Response

The sensitivity to disturbances (i.e. x_f , f_t and f_s) are shown in Figure 2.2. The *plant* (i.e. the transfer function from actuator force f to measured displacement d) is shown in Figure 2.3.

Important

For further analysis, 9 configurations are considered: three nano-hexapod stiffnesses ($k_n = 0.01\text{ N}/\mu\text{m}$, $k_n = 1\text{ N}/\mu\text{m}$ and $k_n = 100\text{ N}/\mu\text{m}$) combined with three sample's masses ($m_s = 1\text{ kg}$, $m_s = 25\text{ kg}$ and $m_s = 50\text{ kg}$).

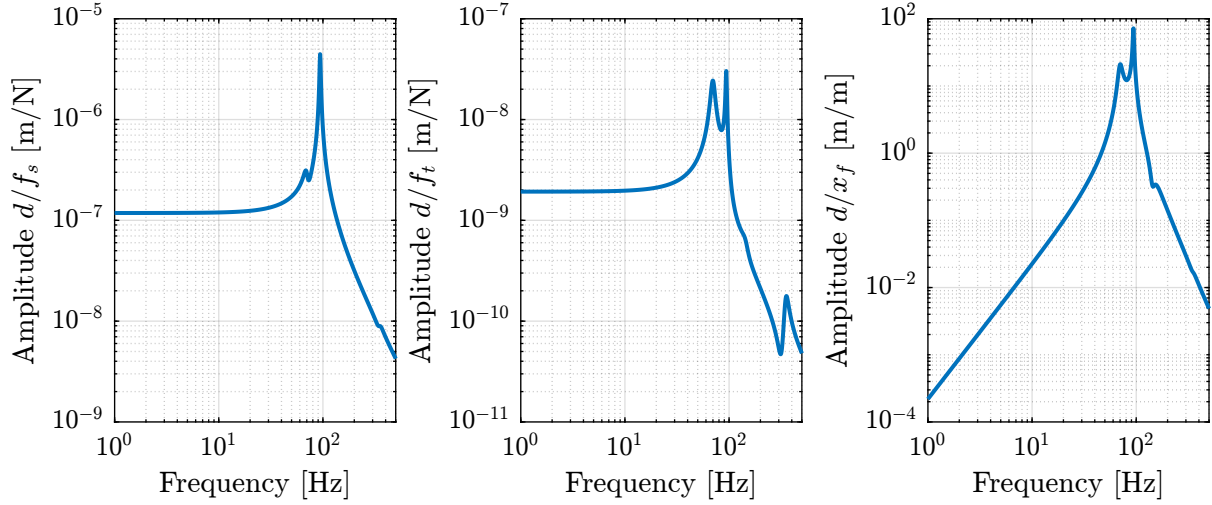


Figure 2.2: Sensitivity of the relative motion d to disturbances: f_s the direct forces applied on the sample, f_t disturbances from the micro-station stages and x_f the floor motion (from left to right)

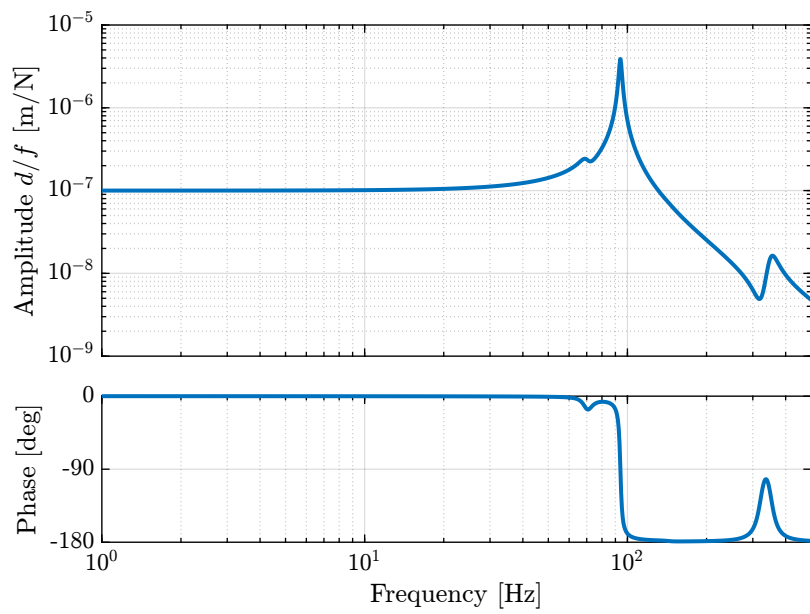


Figure 2.3: Bode Plot of the transfer function from actuator forces to measured displacement by the metrology

3 Disturbance Identification

In order to measure disturbances, two geophones are used, one located on the floor and one on the micro-hexapod's top platform (see Figure 3.1).

The geophone on the floor is used to measure the floor motion x_f while the geophone on the micro-hexapod is used to measure vibrations introduced by scanning of the T_y stage and R_z stage.

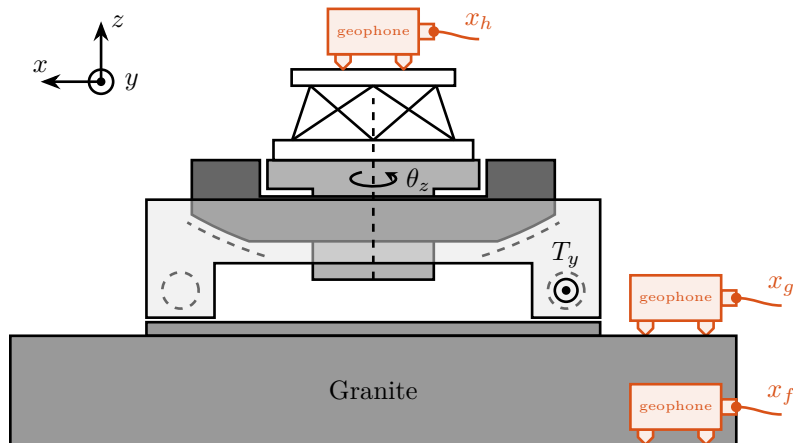


Figure 3.1: Disturbance measurement setup - Schematic

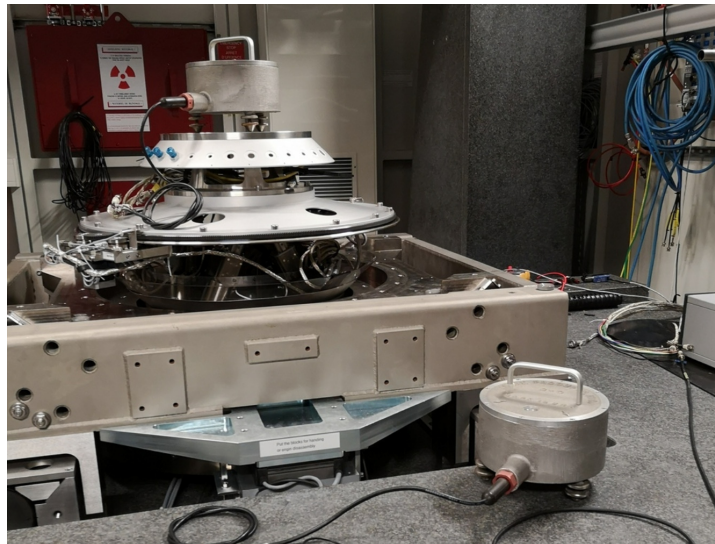


Figure 3.2: Two geophones are used to measure the micro-station vibrations induced by the scanning of the T_y and R_z stages

3.1 Ground Motion

The geophone fixed to the floor to measure the floor motion.

The voltage generated by each geophone is amplified using a voltage amplifier (gain of 60dB) before going to the ADC. The sensitivity of the geophone as well as the gain of the voltage amplifier are then taken into account to reconstruct the floor displacement. The PSD S_{V_f} of the measured voltage V_f is computed. The PSD of the corresponding displacement can be computed as follows:

$$S_{x_f}(\omega) = \frac{S_{V_f}(\omega)}{|S_{\text{geo}}(j\omega)| \cdot G_{\text{amp}} \cdot \omega} \tag{3.1}$$

with:

- S_{geo} the sensitivity of the Geophone in $[Vs/m]$
- G_{amp} the gain of the voltage amplifier
- ω is here to integrate and have the displacement instead of the velocity

The amplitude spectral density Γ_{x_f} of the measured displacement x_f is shown in Figure 3.3.

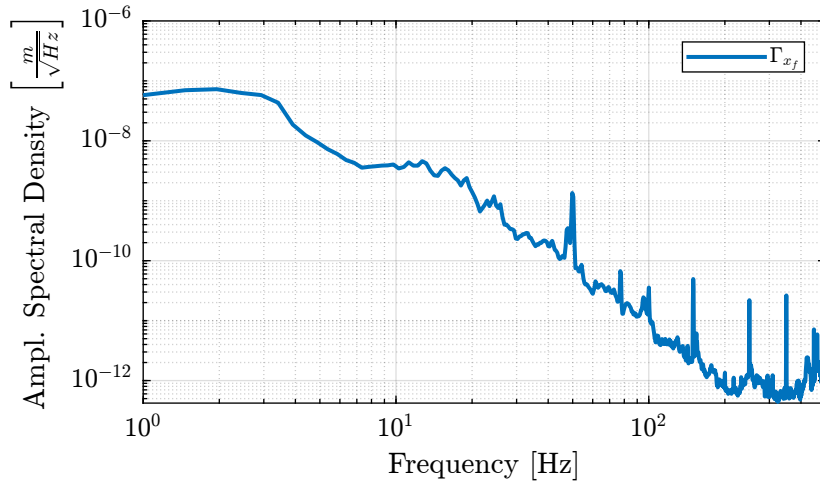


Figure 3.3: Amplitude Spectral Density of the measured Floor motion on ID31

3.2 Stage Vibration

During Spindle rotation (here at 6rpm), the granite velocity and micro-hexapod’s top platform velocity are measured with the geophones.

The Power Spectral Density of the relative velocity between the hexapod and the granite is computed. It is then integrated to obtain the Amplitude Spectral Density of the relative motion which is compared with a non-rotating case (Figure 3.4). It is shown that the spindle rotation induces vibrations in a wide frequency spectrum.

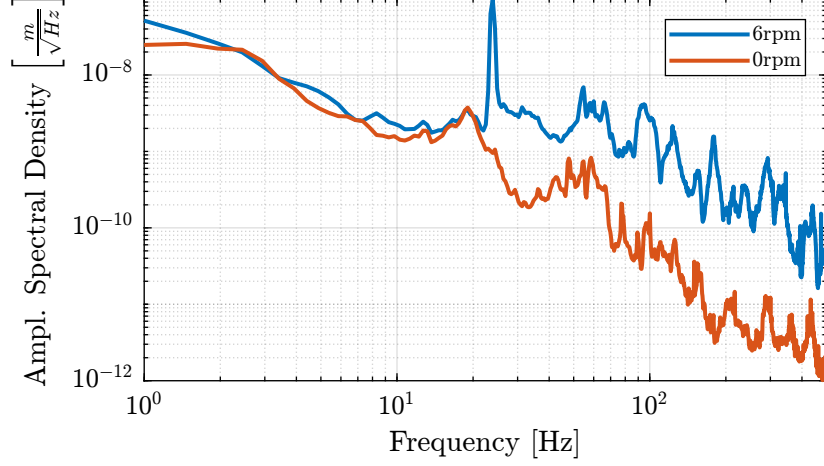


Figure 3.4: Amplitude Spectral Density of the relative motion measured between the granite and the micro-hexapod's top platform during Spindle rotating

In order to compute the equivalent disturbance force f_t that induces such motion, the transfer function from f_t to the relative motion of the hexapod's top platform and the granite is extracted from the model. The power spectral density Γ_{f_t} of the disturbance force can be computed as follows:

$$\Gamma_{f_t}(\omega) = \frac{\Gamma_{v_t}(\omega)}{|G_{\text{model}}(j\omega)|^2} \quad (3.2)$$

with:

- Γ_{v_t} the measured power spectral density of the relative motion between the micro-hexapod's top platform and the granite during the spindle's rotation
- G_{model} the transfer function (extracted from the uniaxial model) from f_t to the relative motion between the micro-hexapod's top platform and the granite

The obtained amplitude spectral density of the disturbance force f_t is shown in Figure 3.5.

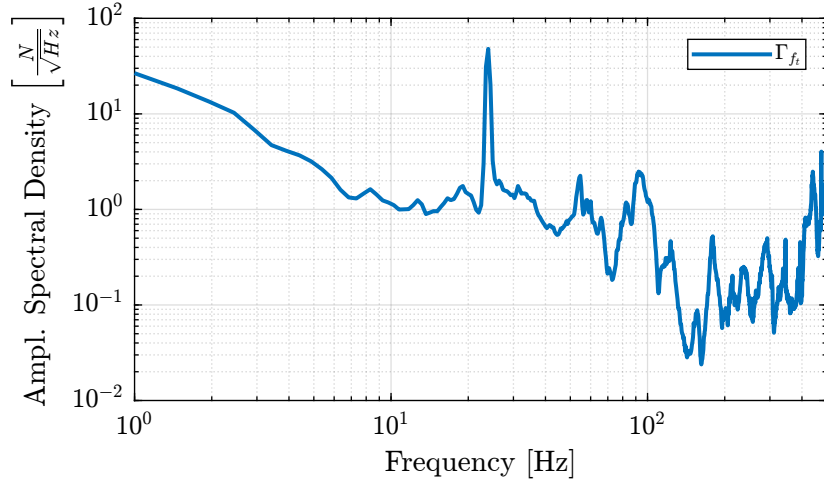


Figure 3.5: Estimated disturbance force f_t from measurement and uniaxial model

The vibrations induced by the T_y stage are not considered here because:

- the induced vibrations have less amplitude than the vibrations induced by the R_z stage
- it can be scanned at lower velocities if the induced vibrations are an issue

4 Open-Loop Dynamic Noise Budgeting

Now that we have a model of the NASS and an estimation of the power spectral density of the disturbances, it is possible to perform an *open-loop dynamic noise budgeting*.

4.1 Sensitivity to disturbances

From the Uni-axial model, the transfer function from the disturbances (f_s , x_f and f_t) to the displacement d are computed.

This is done for **two extreme sample masses** $m_s = 1$ kg and $m_s = 50$ kg and **three nano-hexapod stiffnesses**:

- $k_n = 0.01$ N/ μ m that could represent a voice coil actuator with soft flexible guiding
- $k_n = 1$ N/ μ m that could represent a voice coil actuator with a stiff flexible guiding or a mechanically amplified piezoelectric actuator
- $k_n = 100$ N/ μ m that could represent a stiff piezoelectric stack actuator

The obtained sensitivity to disturbances for the three nano-hexapod stiffnesses are shown in Figure 4.1 for the light sample (same conclusions can be drawn with the heavy one).

Important

From Figure 4.1, the following can be concluded for the **soft nano-hexapod**:

- It is more sensitive to forces applied on the sample (cable forces for instance), which is expected due to the lower stiffness
- Between the suspension mode of the nano-hexapod (here at 5Hz) and the first mode of the micro-station (here at 70Hz), the disturbances induced by the stage vibrations are filtered out.
- Above the suspension mode of the nano-hexapod, the sample's motion is unaffected by the floor motion, and therefore the sensitivity to floor motion is close to 1.

4.2 Open-Loop Dynamic Noise Budgeting

Now, the power spectral density of the disturbances is taken into account to estimate the residual motion d in each case.

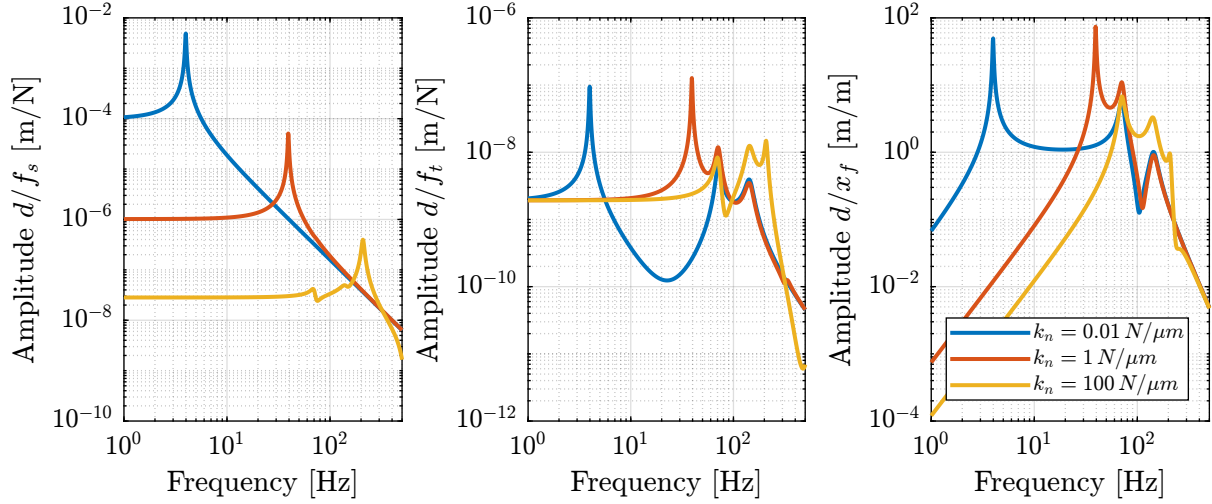


Figure 4.1: Sensitivity to disturbances for three different nano-hexpod stiffnesses

The Cumulative Amplitude Spectrum of the relative motion d due to both the floor motion x_f and the stage vibrations f_t are shown in Figure 4.2 for the three nano-hexpod stiffnesses.

It is shown that the effect of the floor motion is much less than the stage vibrations, except for the soft nano-hexapod below 5Hz.

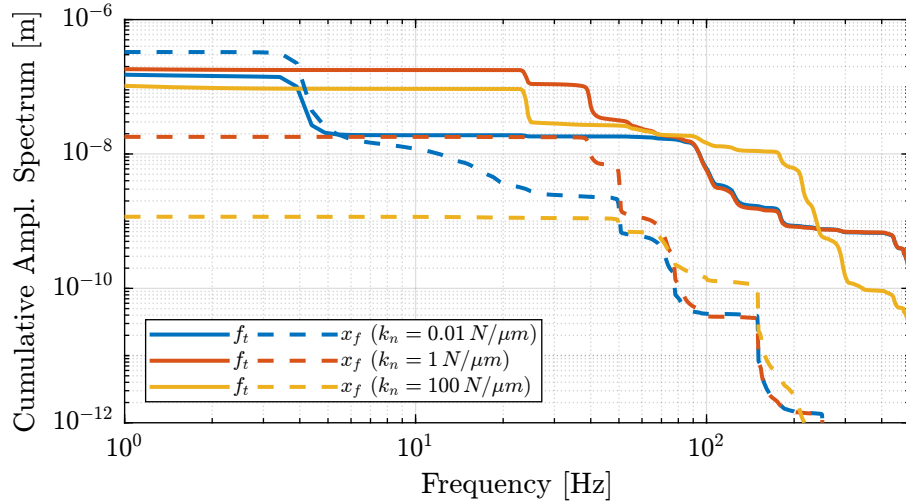


Figure 4.2: Cumulative Amplitude Spectrum of the relative motion d , due to both the floor motion and the stage vibrations (light sample)

The total cumulative amplitude spectrum for the three nano-hexpod stiffnesses and for the two sample's masses are shown in Figure 4.3. The conclusion is that the sample's mass has little effect on the cumulative amplitude spectrum of the relative motion d .

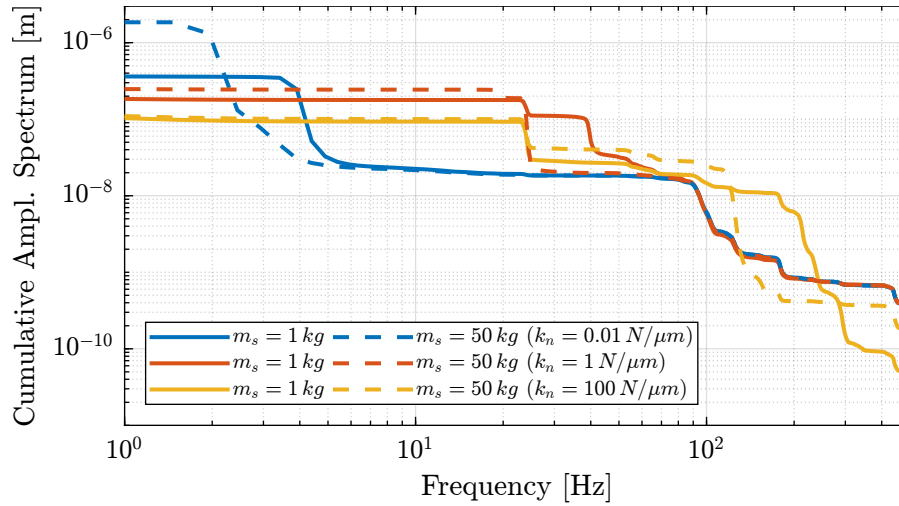


Figure 4.3: Cumulative Amplitude Spectrum of the relative motion d due to all disturbances, for two sample masses

Conclusion

Important

In order to have a closed-loop residual vibration $d \approx 20 \text{ nm}$ rms, if a simple feedback controller is used, the required closed-loop bandwidth would be:

- $\approx 10 \text{ Hz}$ for the soft nano-hexapod ($k_n = 0.01 \text{ N}/\mu\text{m}$)
- $\approx 50 \text{ Hz}$ for the relatively stiff nano-hexapod ($k_n = 1 \text{ N}/\mu\text{m}$)
- $\approx 100 \text{ Hz}$ for the stiff nano-hexapod ($k_n = 100 \text{ N}/\mu\text{m}$)

This can be explained by the fact that for frequencies larger than the suspension mode of the nano-hexapod, the stage vibrations are filtered out (see Figure 4.1).

This gives a first advantage to having a soft nano-hexapod.

5 Active Damping

In this section, three active damping are applied on the nano-hexapod (see Figure 5.1): Integral Force Feedback (IFF) [1], Relative Damping Control (RDC) [2, Chapter 7.2] and Direct Velocity Feedback (DVF) [3]–[5].

These damping strategies will be described in Section 5.1.

These active damping techniques are compared in terms of:

- Achievable damping of the nano-hexapod mode (Section 5.3)
- Reduction of the effect of disturbances (i.e. x_f , f_t and f_s) on the displacement d (Sections 5.4 and 5.5)
- Robustness to a change of sample's mass (Section 5.7)

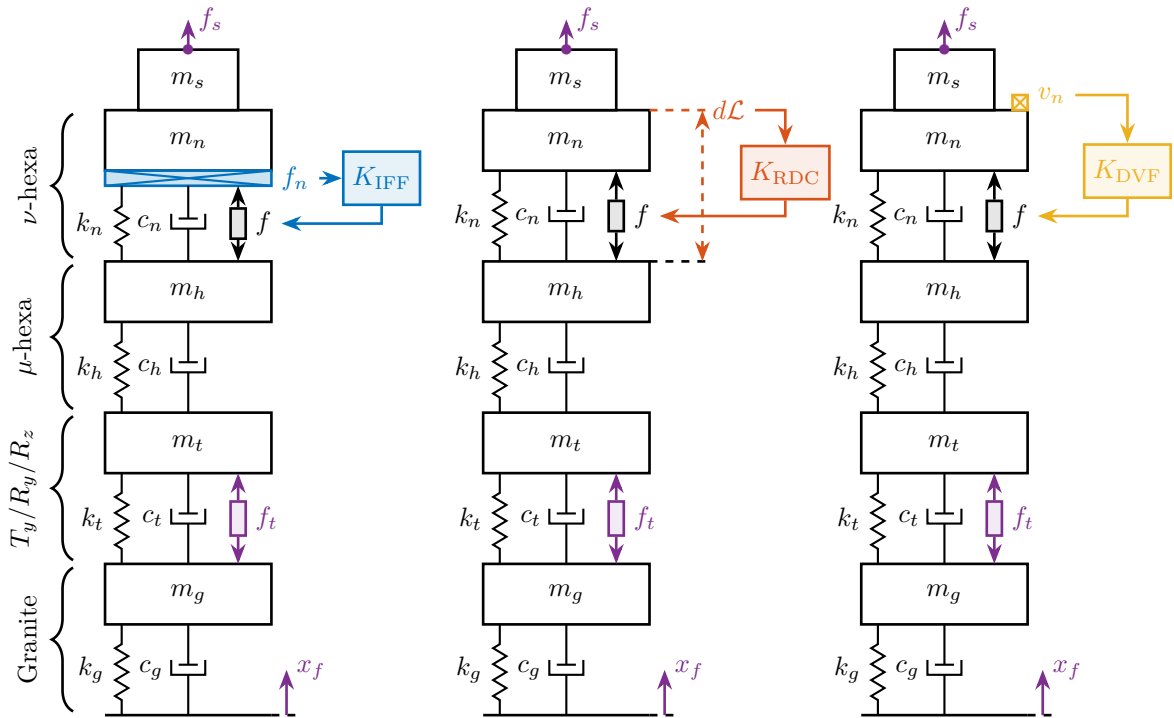


Figure 5.1: Three active damping strategies: Integral Force Feedback (IFF) using a force sensor, Relative Damping Control (RDC) using a relative displacement sensor, and Direct Velocity Feedback (DVF) using a geophone

5.1 Active Damping Strategies

Integral Force Feedback (IFF) The Integral Force Feedback strategy consists of using a force sensor in series with the actuator (see Figure 5.2, left).

The control strategy consists of integrating the measured force and feeding it back to the actuator:

$$K_{\text{IFF}}(s) = \frac{g}{s} \quad (5.1)$$

The mechanical equivalent of this strategy is to add a dashpot in series with the actuator stiffness with a damping coefficient equal to the stiffness of the actuator divided by the controller gain k/g (see Figure 5.2, right).

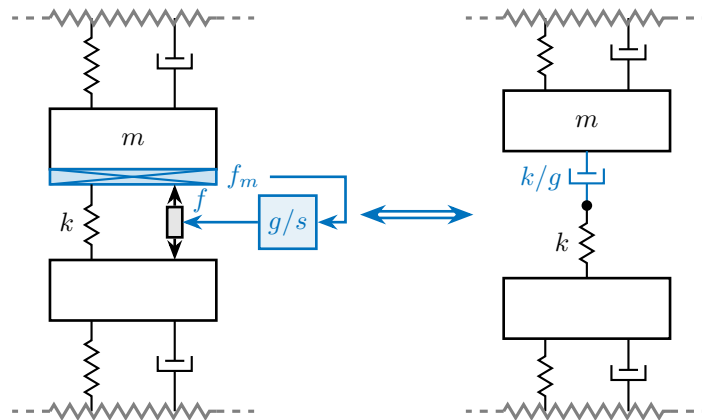


Figure 5.2: Integral Force Feedback is equivalent as to add a damper in series with the stiffness (the initial damping is here neglected for simplicity)

Relative Damping Control (RDC) For the Relative Damping Control strategy, a relative motion sensor that measures the motion of the actuator is used (see Figure 5.3, left).

The derivative of this relative motion is used for the feedback signal:

$$K_{\text{RDC}}(s) = -g \cdot s \quad (5.2)$$

The mechanical equivalent is to add a dashpot in parallel with the actuator with a damping coefficient equal to the controller gain g (see Figure 5.3, right).

Direct Velocity Feedback (DVF) Finally, the Direct Velocity Feedback strategy consists of using an inertial sensor (usually a geophone), that measured the “absolute” velocity of the body fixed on top of the actuator (see Figure 5.4, left).

The measured velocity is then fed back to the actuator:

$$K_{\text{DVF}}(s) = -g \quad (5.3)$$

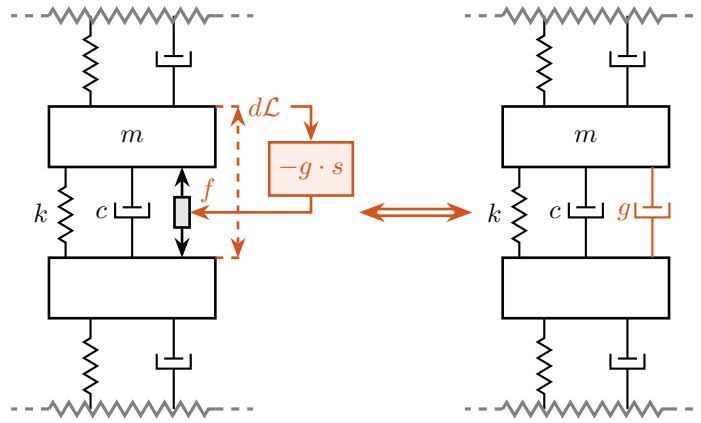


Figure 5.3: Relative Damping Control is equivalent as adding a damper in parallel with the actuator/relative motion sensor

This is equivalent as to fix a dashpot (with a damping coefficient equal to the controller gain g) between the body (one which the inertial sensor is fixed) and an inertial reference frame (see Figure 5.4, right). This is usually refers to as “sky hook damper”.

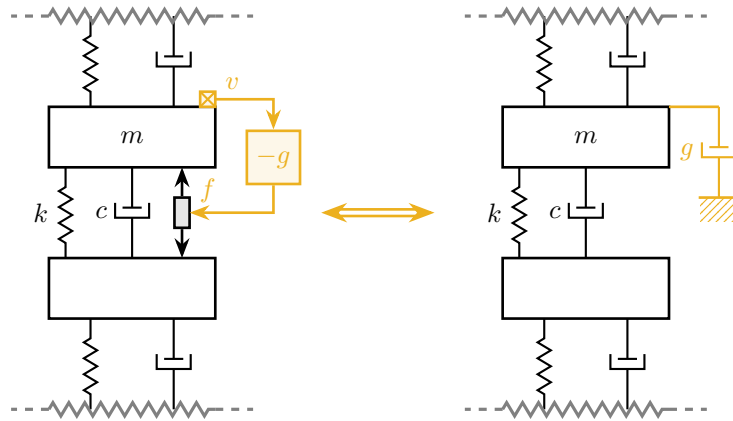


Figure 5.4: Direct velocity Feedback using an inertial sensor is equivalent to a “sky hook damper”

5.2 Plant Dynamics for Active Damping

The plant dynamics for all three active damping techniques are shown in Figure 5.5. All have **alternating poles and zeros** meaning that the phase do not vary by more than ± 90 deg which makes the design of a robust controller very easy. The reason all three plants in Figure 5.5 have alternating poles and zeros is because the three sensors are all collocated with the actuator [2, Chapter 7].

When the nano-hexapod’s suspension modes are at lower frequencies than the resonances of the micro-station (blue and red curves in Figure 5.5), the resonances of the micro-stations have little impact on the IFF and DVF transfer functions.

For the stiff nano-hexapod (yellow curves), the micro-station dynamics can be seen on the transfer functions in Figure 5.5. Therefore, it is expected that the micro-station dynamics might impact the

achievable damping if a stiff nano-hexapod is used.

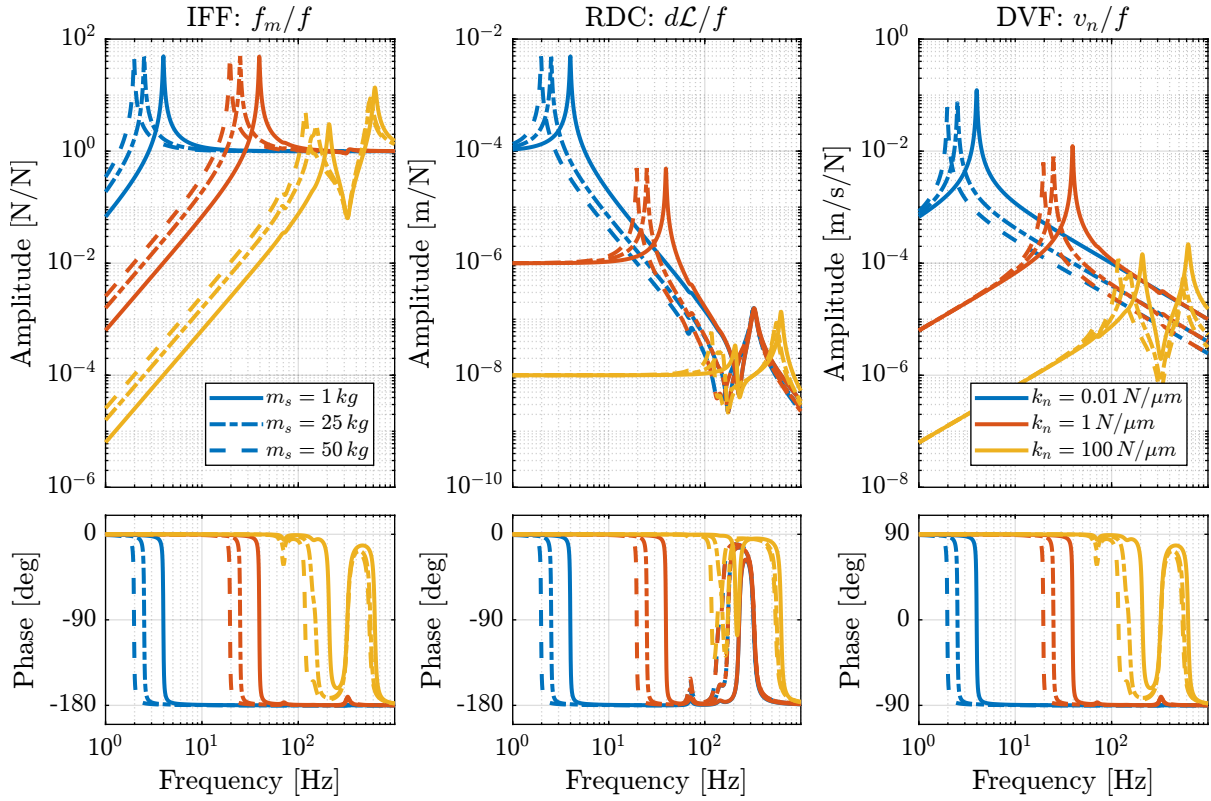


Figure 5.5: Plant dynamics for the three active damping techniques (IFF: right, RDC: middle, DVF: left), for three nano-hexapod stiffnesses ($k_n = 0.01 N/\mu m$ in blue, $k_n = 1 N/\mu m$ in red and $k_n = 100 N/\mu m$ in yellow) and three sample’s masses ($m_s = 1 kg$: solid curves, $m_s = 25 kg$: dot-dashed curves, and $m_s = 50 kg$: dashed curves).

5.3 Achievable Damping - Root Locus

The Root Locus are computed for the three nano-hexapod stiffnesses and for the three active damping techniques. They are shown in Figure 5.6.

All three active damping approach can lead to **critical damping** of the nano-hexapod suspension mode.

There is even some damping authority on micro-station modes in the following cases:

IFF with a stiff nano-hexapod (Figure 5.6, right) This can be understood from the mechanical equivalent of IFF shown in Figure 5.2 (right) considering an high stiffness k . The micro-station top platform is connected to an inertial mass (the nano-hexapod) through a damper, which damps the micro-station suspension suspension mode.

DVF with a stiff nano-hexapod (Figure 5.6, right) In that case, the “sky hook damper” (see mechanical equivalent of IFF in Figure 5.4, right) is connected to the micro-station top platform through the stiff nano-hexapod.

RDC with a soft nano-hexapod (Figure 5.7) At the frequency of the micro-station mode, the nano-hexapod top mass is behaving as an inertial reference as the suspension mode of the soft nano-hexapod is at much lower frequency. The micro-station and the nano-hexapod masses are connected through a large damper induced by RDC (see mechanical equivalent in Figure 5.3, right) which allows some damping of the micro-station.

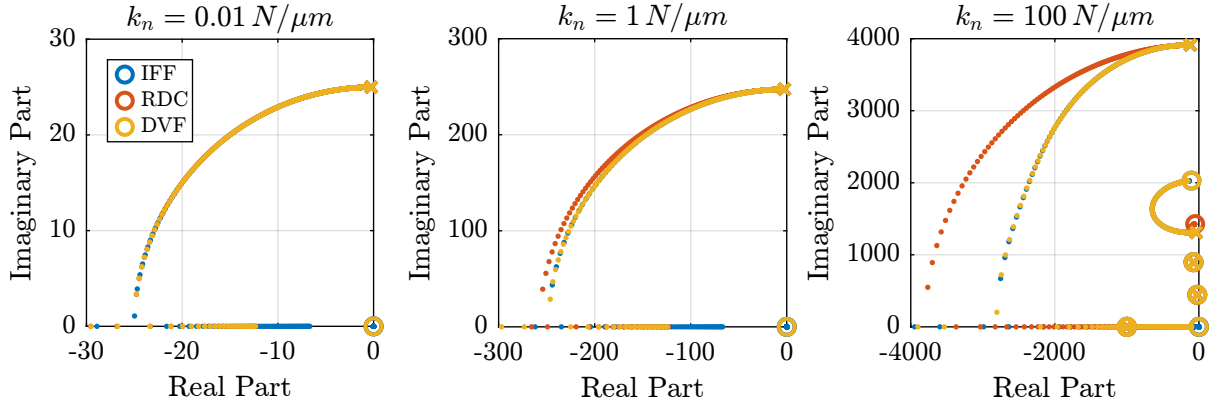


Figure 5.6: Root Loci for the three active damping techniques (IFF in blue, RDC in red and DVF in yellow). This is shown for three nano-hexapod stiffnesses. The Root Loci are zoomed on the suspension mode of the nano-hexapod.

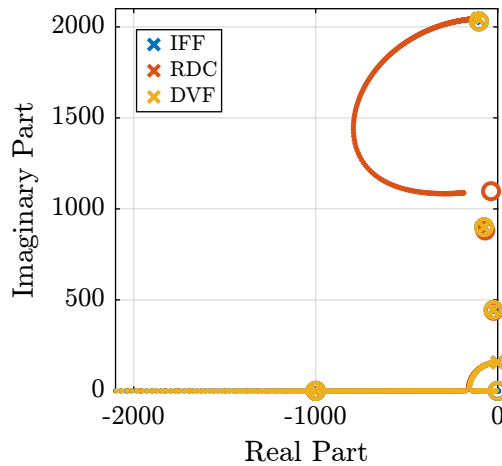


Figure 5.7: Root Locus for the three damping techniques applied with the soft nano-hexapod. It is shown that the RDC active damping technique has some authority on one mode of the micro-station. This mode corresponds to the suspension mode of the micro-hexapod.

5.4 Change of sensitivity to disturbances

The sensitivity to disturbances (direct forces f_s , stage vibrations f_t and floor motion x_f) for all three active damping techniques are compared in Figure 5.8. The comparison is done with the nano-hexapod having a stiffness $k_n = 1 N/\mu m$.

Important

Conclusions from Figure 5.8 are:

- IFF degrades the sensitivity to direct forces on the sample (i.e. the compliance) below the resonance of the nano-hexapod
- RDC degrades the sensitivity to stage vibrations around the nano-hexapod's resonance as compared to the other two methods
- both IFF and DVF degrades the sensitivity to floor motion below the resonance of the nano-hexapod

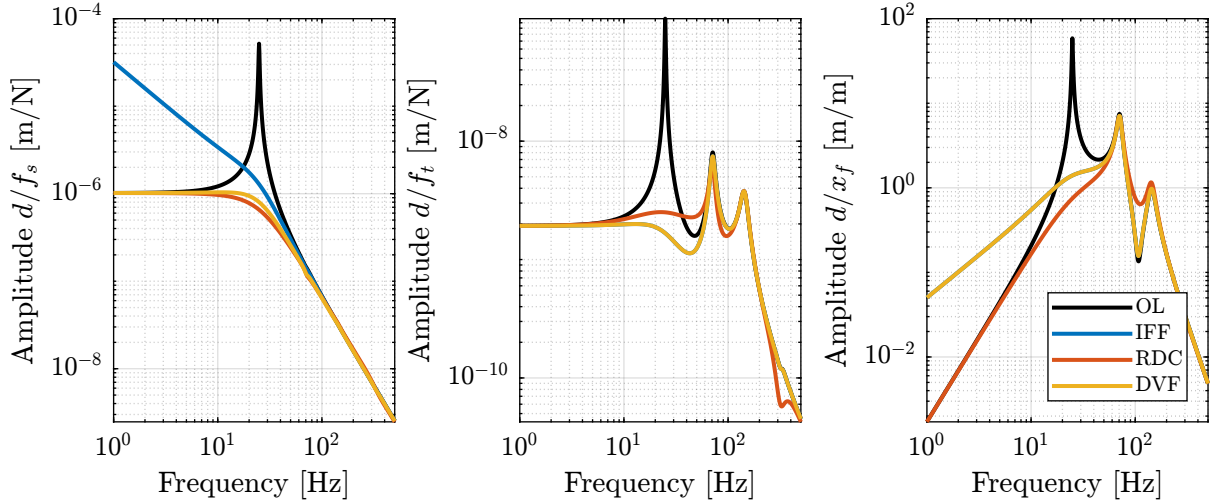


Figure 5.8: Change of sensitivity to disturbance with all three active damping strategies

5.5 Noise Budgeting after Active Damping

Cumulative Amplitude Spectrum of the distance d with all three active damping techniques are compared in Figure 5.9. All three active damping methods are giving similar results (except the RDC which is a little bit worse for the stiff nano-hexapod).

Compared to the open-loop case, the active damping helps to lower the vibrations induced by the nano-hexapod resonance.

5.6 Obtained Closed Loop Response

The transfer functions from the plant input f to the relative displacement d while the active damping is implemented are shown in Figure 5.10. All three active damping techniques yield similar damped plants.

The damped plants are shown in Figure 5.11 for all three techniques, with the three considered nano-hexapod stiffnesses and sample's masses.

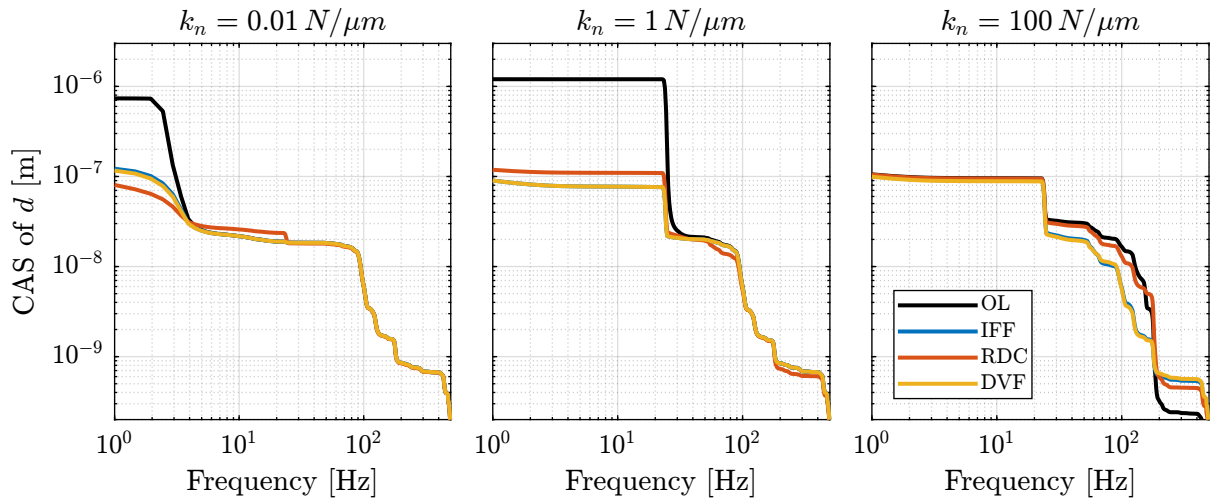


Figure 5.9: Comparison of the cumulative amplitude spectrum (CAS) of the distance d for all three active damping techniques (OL in black, IFF in blue, RDC in red and DVF in yellow).

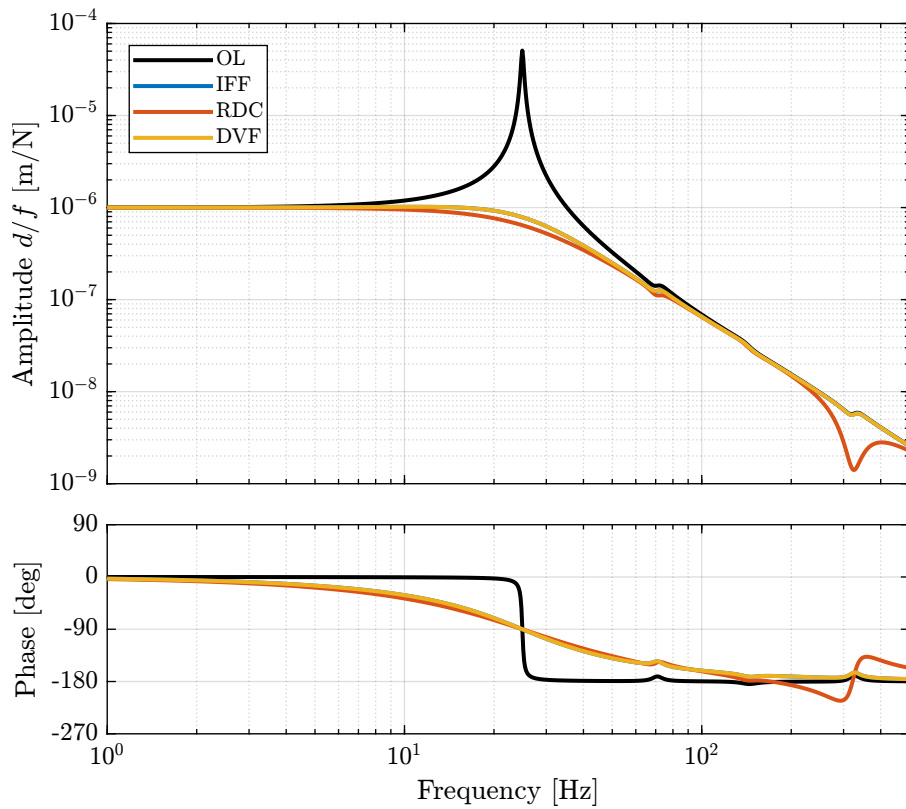


Figure 5.10: Obtained damped transfer function from f to d for the three damping techniques

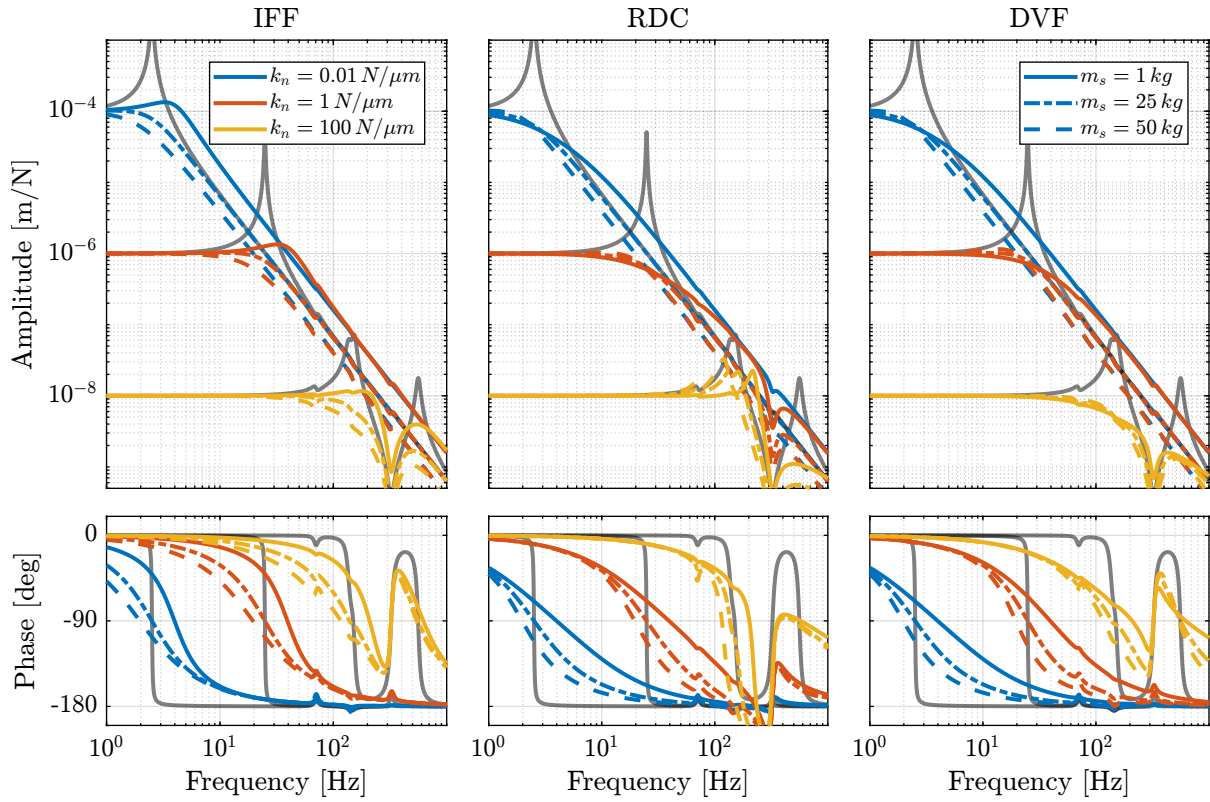


Figure 5.11: Damped plant d/f - Robustness to change of sample's mass for all three active damping techniques. Grey curves are the open-loop (i.e. undamped) plants.

5.7 Robustness to change of payload's mass

The Root Locus for the three damping techniques are shown in Figure 5.12 for three sample's mass (1kg, 25kg and 50kg). The closed-loop poles are shown by the squares for a specific gain.

We can see that having heavier samples yields larger damping for IFF and smaller damping for RDC and DVF.

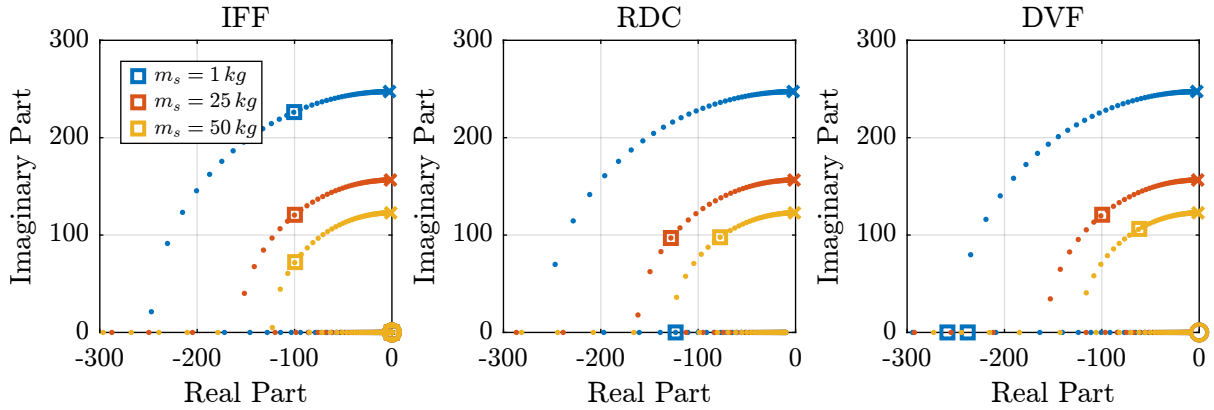


Figure 5.12: Active Damping Robustness to change of sample's mass - Root Locus for all three damping techniques with 3 different sample's masses

Conclusion

Important

Conclusions for Active Damping:

- All three active damping techniques yields good damping (Figure 5.6) and similar remaining vibrations (Figure 5.9)
- The obtained damped plants (Figure 5.11) are equivalent for the three active damping techniques
- Which one to be used will be determined with the use of more accurate models and will depend on which is the easiest to implement in practice

Table 5.1: Comparison of active damping strategies

	IFF	RDC	DVF
Sensor	Force sensor	Relative motion sensor	Inertial sensor
Damping	Up to critical	Up to critical	Up to Critical
Robustness	Requires collocation	Requires collocation	Impacted by geophone resonances
f_s Disturbance	↗ at low frequency	↘ near resonance	↘ near resonance
f_t Disturbance	↘ near resonance	↗ near resonance	↘ near resonance
x_f Disturbance	↗ at low frequency	↘ near resonance	↗ at low frequency

6 Position Feedback Controller

The High Authority Control - Low Authority Control (HAC-LAC) architecture is shown in Figure 6.1a. It corresponds to a *two step* control strategy:

- First, an active damping controller \mathbf{K}_{LAC} is implemented (see Section 5). It allows to reduce the vibration level, and it also makes the damped plant (transfer function from u' to y) easier to control than the undamped plant (transfer function from u to y).
- Then, a position controller \mathbf{K}_{HAC} is implemented which is used to control the position d .

When applied on the uniaxial model with IFF used as the Low Authority Control, the schematic shown in Figure 6.1b is obtained.

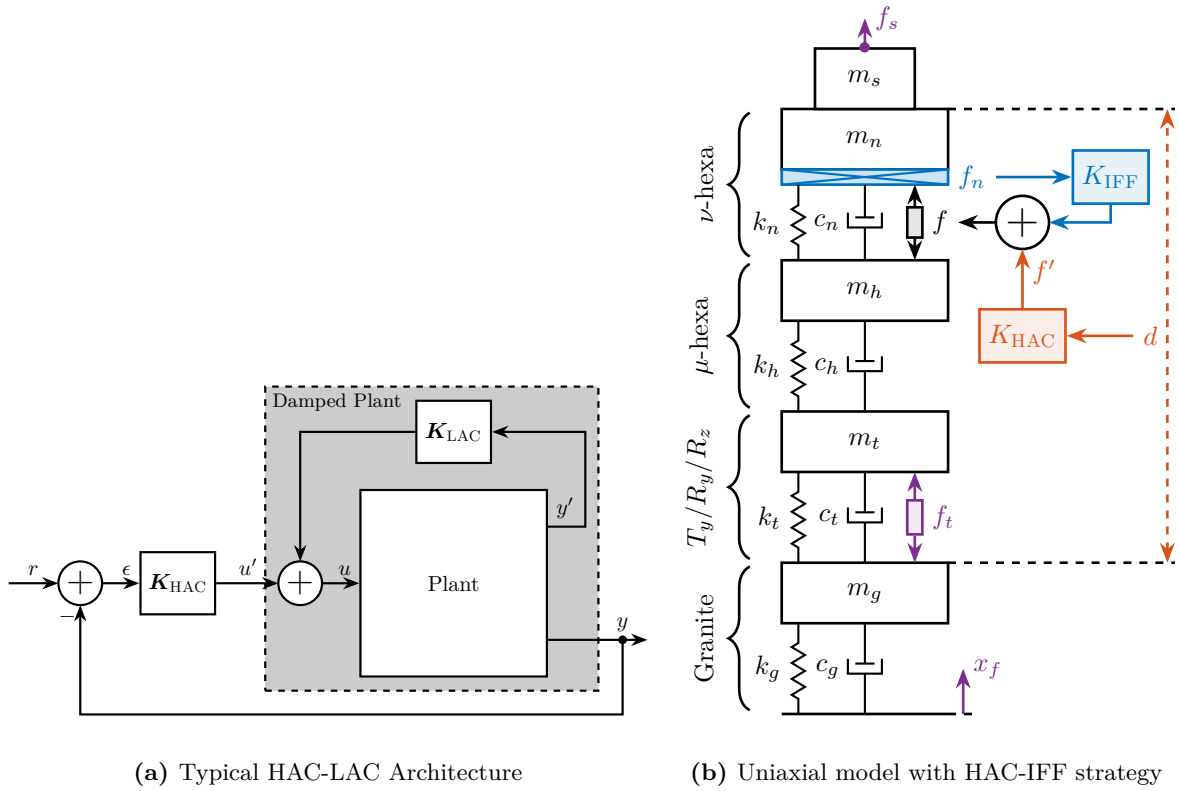


Figure 6.1: High Authority Control - Low Authority Control (HAC-LAC)

6.1 Damped Plant Dynamics

As was shown in Section 5, all three proposed active damping techniques yield similar damping plants. Therefore, *Integral Force Feedback* will be used in this section to study the HAC-LAC performance.

The obtained damped plants for the three nano-hexapod stiffnesses are shown in Figure 6.2. For $k_n = 0.01 N/\mu m$ and $k_n = 1 N/\mu m$, except from the nano-hexapod mode, the dynamics is quite simple and can be well approximated by a second order plant. However, this is not the case for the stiff nano-hexapod ($k_n = 100 N/\mu m$) where two modes can be seen (Figure 6.2, right).

This is due to the interaction between the micro-station (modelled modes at 70Hz, 140Hz and 320Hz) and the nano-hexapod. Such effect will be explained in Section 7.

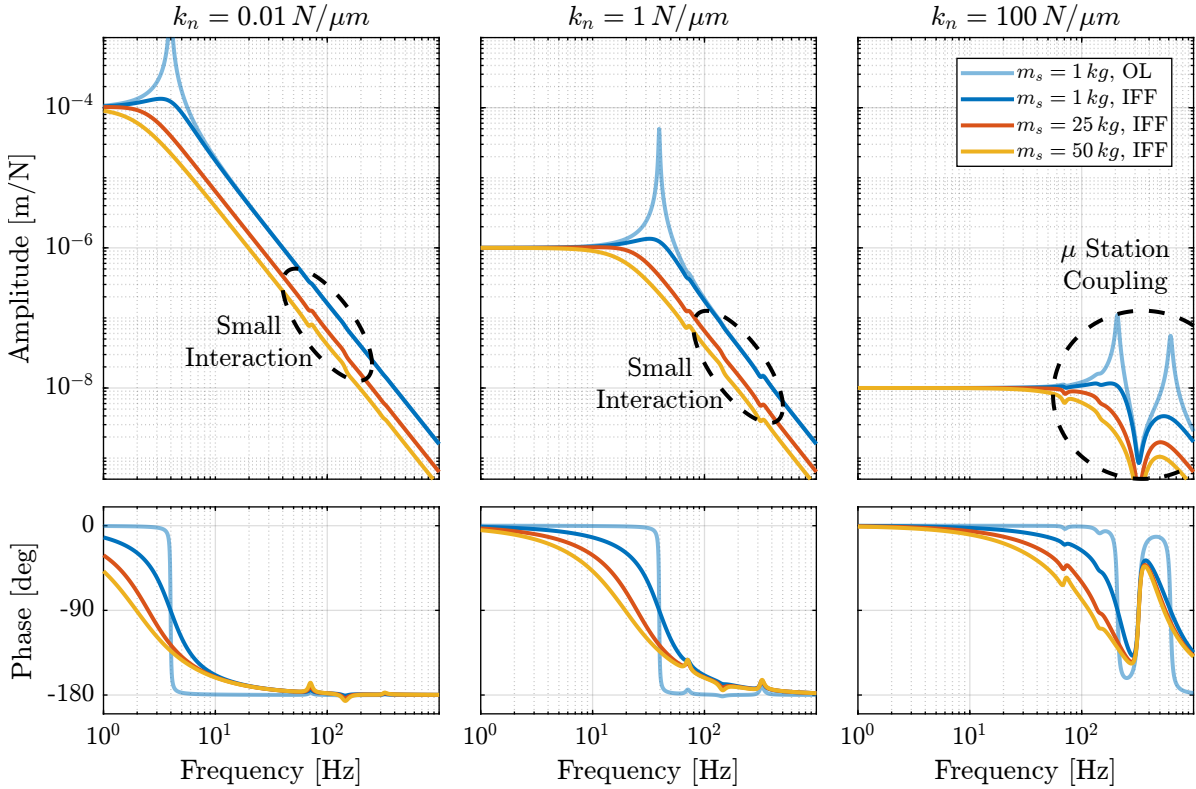


Figure 6.2: Obtained damped plant using Integral Force Feedback for three sample's masses

6.2 Position Feedback Controller

The objective now is to design a position feedback controller for each of the three nano-hexapods that are robust to the change of sample's mass.

The required feedback bandwidth was approximately determined in Section 4:

- ≈ 10 Hz for the soft nano-hexapod ($k_n = 0.01 N/\mu m$). Near this frequency, the plants are equivalent to a mass line. The gain of the mass line can vary up to a fact ≈ 5 (suspended mass from

16 kg up to 65 kg). This means that the designed controller will need to have large gain margins to be robust to the change of sample's mass.

- ≈ 50 Hz for the relatively stiff nano-hexapod ($k_n = 1 \text{ N}/\mu\text{m}$). Similarly to the soft nano-hexapod, the plants near the crossover frequency are equivalent to a mass line. It will be probably easier to have a little bit more bandwidth in this configuration to be further away from the nano-hexapod suspension mode.
- ≈ 100 Hz for the stiff nano-hexapod ($k_n = 100 \text{ N}/\mu\text{m}$). Contrary to the two first nano-hexapod stiffnesses, here the plants have more complex dynamics near the wanted crossover frequency. The micro-station is not stiff enough to have a clear stiffness line at this frequency. Therefore, there are both a change of phase and gain depending on the sample's mass. This makes the robust design of the controller a little bit more complicated.

Position feedback controllers are designed for each nano-hexapod such that it is stable for all considered sample masses with similar stability margins (see Nyquist plots in Figure 6.3). These high authority controllers are generally composed of a lag at low frequency for disturbance rejection, a lead to increase the phase margin near the crossover frequency and a low pass filter to increase the robustness to high frequency dynamics. The controllers used for the three nano-hexapod are shown in Equation (6.1), and the parameters are summarized in Table 6.1.

$$K_{\text{soft}}(s) = g \cdot \underbrace{\frac{s + \omega_0}{s + \omega_i}}_{\text{lag}} \cdot \underbrace{\frac{1 + \frac{s}{\omega_c/\sqrt{a}}}{1 + \frac{s}{\omega_c\sqrt{a}}}}_{\text{lead}} \cdot \underbrace{\frac{1}{1 + \frac{s}{\omega_l}}}_{\text{LPF}} \quad (6.1a)$$

$$K_{\text{mid}}(s) = g \cdot \underbrace{\left(\frac{s + \omega_0}{s + \omega_i}\right)^2}_{2 \text{ lags}} \cdot \underbrace{\frac{1 + \frac{s}{\omega_c/\sqrt{a}}}{1 + \frac{s}{\omega_c\sqrt{a}}}}_{\text{lead}} \cdot \underbrace{\frac{1}{1 + \frac{s}{\omega_l}}}_{\text{LPF}} \quad (6.1b)$$

$$K_{\text{stiff}}(s) = g \cdot \underbrace{\left(\frac{1}{s + \omega_i}\right)^2}_{2 \text{ lags}} \cdot \underbrace{\left(\frac{1 + \frac{s}{\omega_c/\sqrt{a}}}{1 + \frac{s}{\omega_c\sqrt{a}}}\right)^2}_{2 \text{ leads}} \cdot \underbrace{\frac{1}{1 + \frac{s}{\omega_l}}}_{\text{LPF}} \quad (6.1c)$$

Table 6.1: Parameters used for the position feedback controllers

	Soft	Moderately stiff	Stiff
Gain	$g = 4 \cdot 10^5$	$g = 3 \cdot 10^6$	$g = 6 \cdot 10^{12}$
Lead	$a = 5, \omega_c = 20 \text{ Hz}$	$a = 4, \omega_c = 70 \text{ Hz}$	$a = 5, \omega_c = 100 \text{ Hz}$
Lag	$\omega_0 = 5 \text{ Hz}, \omega_i = 0.01 \text{ Hz}$	$\omega_0 = 20 \text{ Hz}, \omega_i = 0.01 \text{ Hz}$	$\omega_i = 0.01 \text{ Hz}$
LPF	$\omega_l = 200 \text{ Hz}$	$\omega_l = 300 \text{ Hz}$	$\omega_l = 500 \text{ Hz}$

The loop gains for the three nano-hexapod are shown in Figure 6.4. We can see that:

- for the soft and moderately stiff nano-hexapod, the crossover frequency varies a lot with the sample mass. This is due to the fact that the crossover frequency corresponds to the mass line of the plant.
- for the stiff nano-hexapod, the obtained crossover frequency is not at high as what was estimated necessary. The crossover frequency in that case is close to the stiffness line of the plant, which makes the robust design of the controller easier.

Note that these controllers were quickly tuned by hand and not designed using any optimization methods. The goal is just to have a first estimation of the attainable performance.

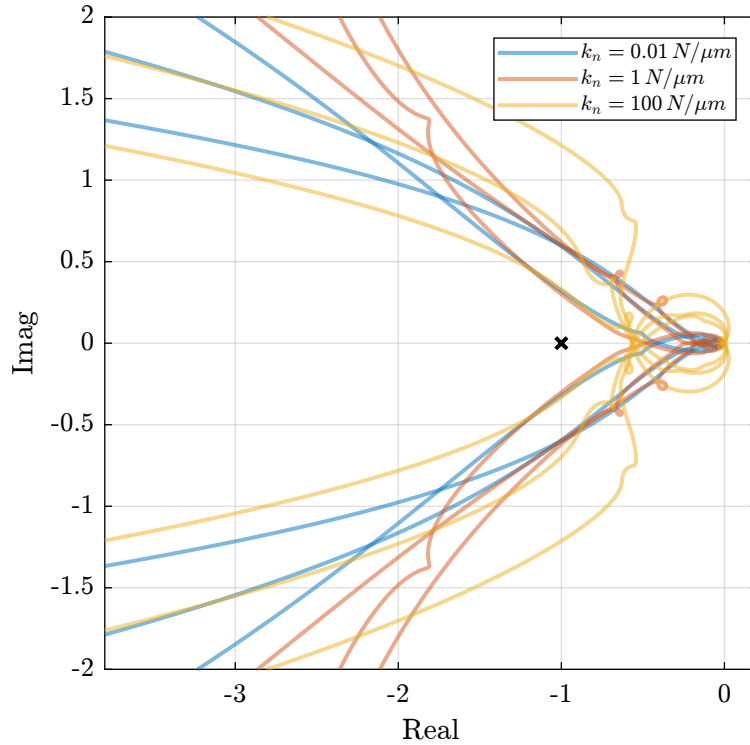


Figure 6.3: Nyquist Plot - Hight Authority Controller for all three nano-hexapod stiffnesses (soft one in blue, moderately stiff in red and very stiff in yellow) and all sample masses (corresponding to the three curves of each color)

6.3 Closed-Loop Noise Budgeting

The high authority position feedback controllers are then implemented and the closed-loop sensitivity to disturbances are computed. These are compared with the open-loop and damped plants cases in Figure 6.5 for just one configuration (moderately stiff nano-hexapod with 25kg sample's mass). As expected, the sensitivity to disturbances is decreased in the controller bandwidth and slightly increase outside this bandwidth.

The cumulative amplitude spectrum of the motion d is computed for all nano-hexapod configurations, all sample masses and in the open-loop (OL), damped (IFF) and position controlled (HAC-IFF) cases. The results are shown in Figure 6.6. Obtained root mean square values of the distance d are better for the soft nano-hexapod ($\approx 25 \text{ nm}$ to $\approx 35 \text{ nm}$ depending on the sample's mass) than for the stiffer nano-hexapod (from $\approx 30 \text{ nm}$ to $\approx 70 \text{ nm}$).

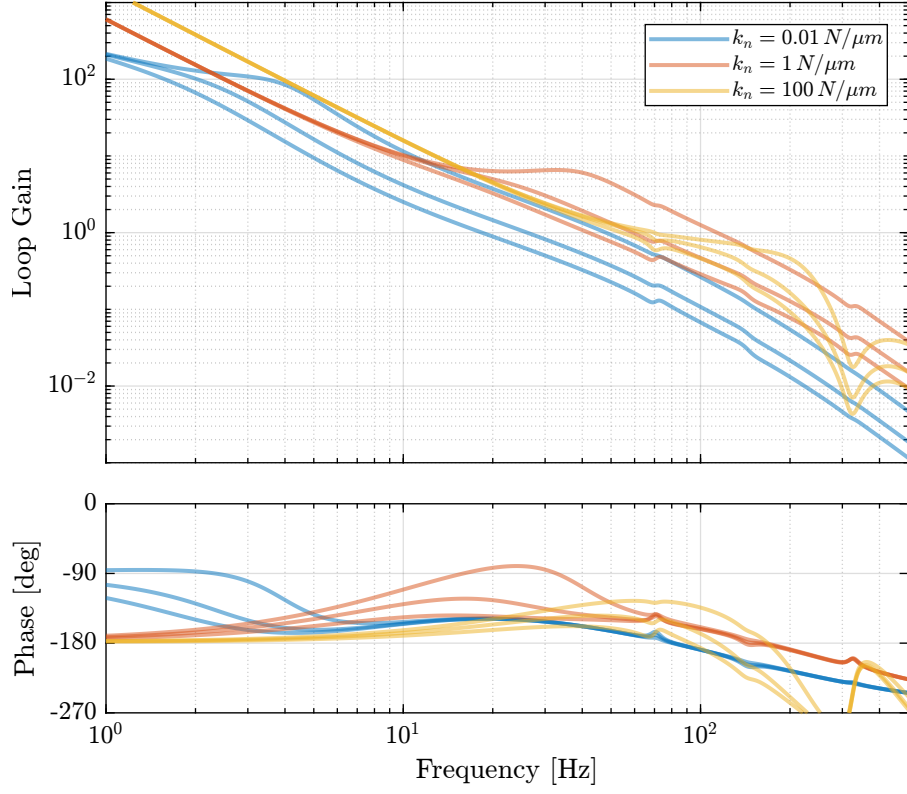


Figure 6.4: Loop Gain - High Authority Controller for all three nano-hexapod stiffnesses (soft one in blue, moderately stiff in red and very stiff in yellow) and all sample masses (corresponding to the three curves of each color)

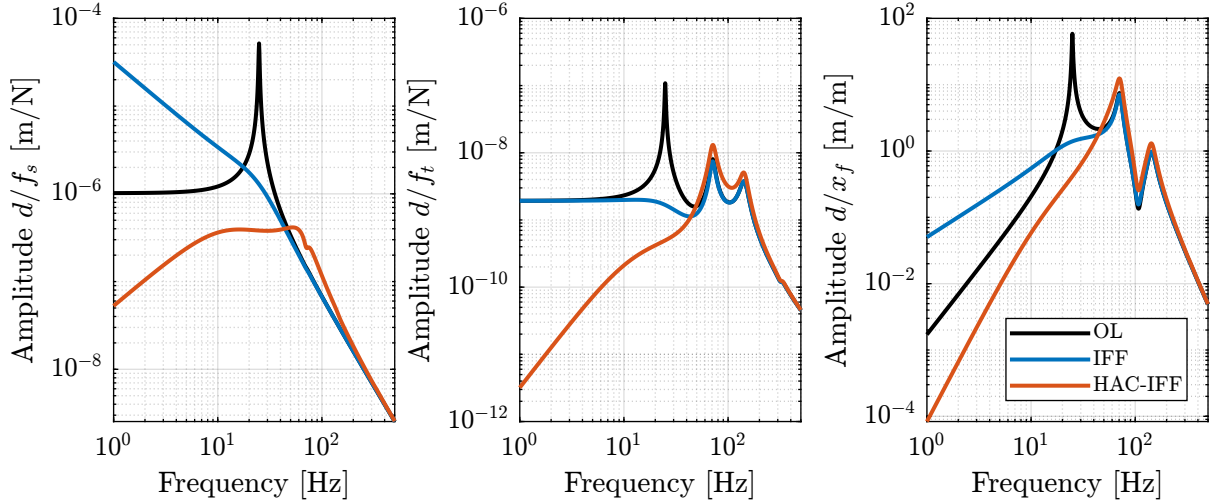


Figure 6.5: Change of sensitivity to disturbances with LAC and with HAC-LAC. Nano-Hexapod with $k_n = 1 \text{ N}/\mu\text{m}$ and sample mass of 25 kg are used.

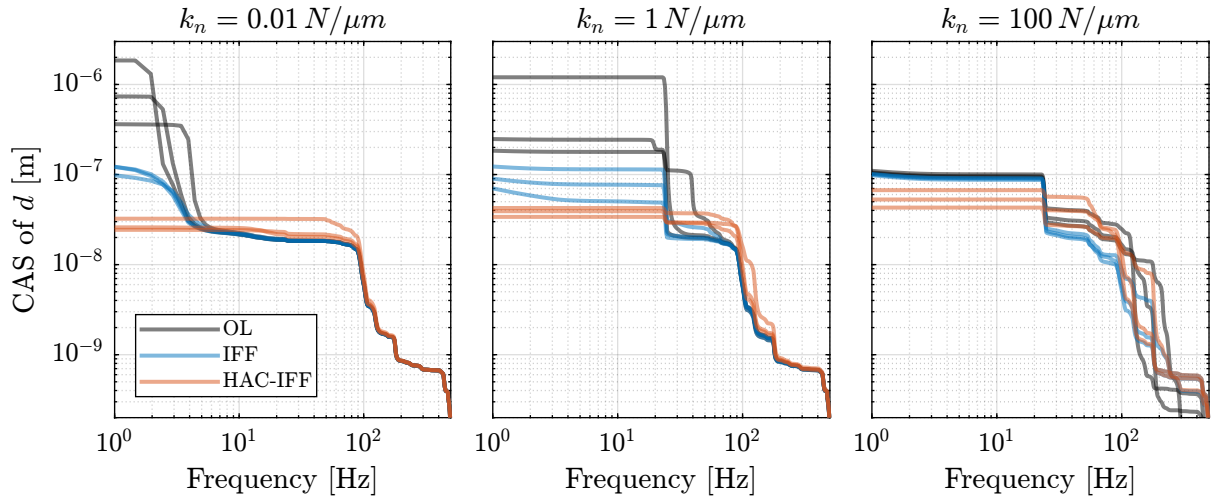


Figure 6.6: Cumulative Amplitude Spectrum for all three nano-hexapod stiffnesses - Comparison of OL, IFF and HAC-LAC cases

Conclusion

Important

Based on the open-loop noise budgeting made in Section 4, the closed-loop bandwidth required to obtain acceptable vibration levels was estimated. In order to obtain such bandwidth, the HAC-LAC strategy was followed which consists of applying an active damping controller and then a high authority position feedback controller.

In this section, feedback controllers were design in such a way that the required closed-loop bandwidth was reached while being robust to a change of payload mass. The attainable vibration control performances were estimated for the three nano-hexapod stiffnesses and were found to be close to the required values. A slight advantage can be given to the soft nano-hexapod as it requires less feedback bandwidth while giving better stability results.

7 Effect of limited micro-station compliance

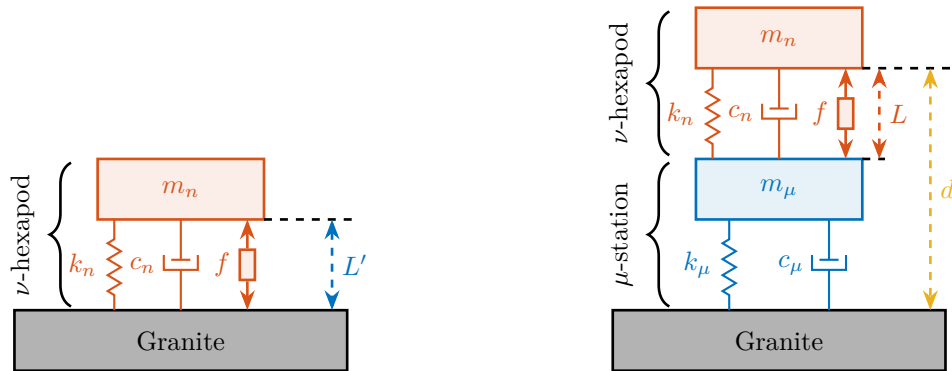
In this section, the impact of the compliance of the support (i.e. the micro-station) on the dynamics of the plant to control will be studied.

This is a critical point as the dynamics of the micro-station is complex, depends on the considered direction (see measurements in Figure 1.3) and may vary with position and time. It would be much better to have a plant dynamics which is not impacted by the micro-station.

Therefore, the objective in this section is to obtain some guidance for the design of a nano-hexapod that will not be impacted by the complex micro-station dynamics.

In order to study this, two models are used (Figure 7.1) with:

- the nano-hexapod directly fixed on top of the granite, therefore neglecting any support compliance (Figure 7.1a)
- the nano-hexapod fixed on top of the micro-station having some limited compliance (Figure 7.1b)



(a) Nano-Hexapod fixed directly on the Granite (b) Nano-Hexapod fixed on top of the Micro-Station

Figure 7.1: Models used to study the effect of limited support compliance

7.1 Neglected support compliance

Let's first neglect the limited compliance of the micro-station and use the uniaxial model show in Figure 7.1a. Let's choose a nano-hexapod mass (including the payload) of 20 kg and three hexapod stiffnesses such that their resonance frequencies are at $\omega_\nu = 10$ Hz, $\omega_\nu = 70$ Hz and $\omega_\nu = 400$ Hz.

The obtained transfer functions from F to L' are shown in Figure 7.2. When neglecting the support compliance, large feedback bandwidth can be achieve for all three Nano-Hexapod.

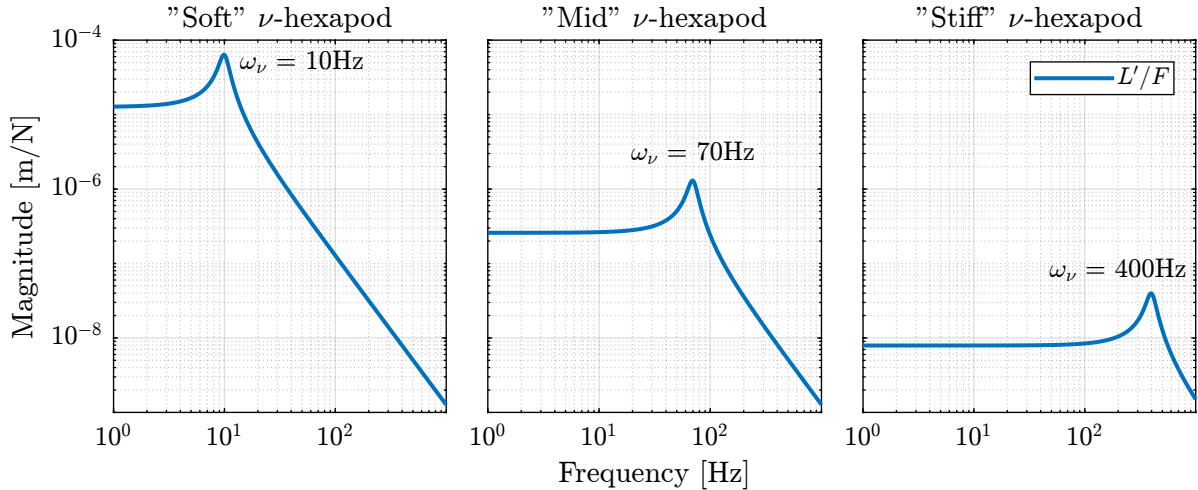


Figure 7.2: Obtained transfer functions from F to L' when neglecting support compliance

7.2 Effect of support compliance on L/F

Let's now add some support compliance and use the model shown in Figure 7.1b. The parameters of the support (i.e. m' , c' and k') are chosen in such a way that the main vertical mode at $\omega_\mu = 70$ Hz seen on the micro-station is matched (Figure 1.3, yellow curve).

The transfer functions from F to L (i.e. control of the relative motion of the nano-hexapod) and from L to d (i.e. control of the position between the nano-hexapod and the fixed granite) can then be computed.

When the relative displacement of the nano-hexapod L is to be controlled (dynamics shown in Figure 7.3), having a stiff nano-hexapod (i.e. with a suspension mode at higher frequency than the mode of the support) makes the dynamics less affected by the limited support compliance (Figure 7.3, right).

This is why it is very common to have stiff piezoelectric stages fixed at the very top of positioning stages. In such case, the control of the piezoelectric stage using its integrated metrology (typically capacitive sensors) is quite simple as the plant is not much affected by the dynamics of the support on which it is fixed. If a soft nano-hexapod is used, the support dynamics appears in the dynamics between F and L (see Figure 7.3, left) which will impact the control robustness and performance.

7.3 Effect of support compliance on d/F

When the motion to be controlled is the relative displacement d between the granite and the nano-hexapod's top platform, the effect of the support compliance on the plant dynamics is opposite than what was previously observed. Indeed, using a "soft" nano-hexapod (i.e. with a suspension mode at lower frequency than the mode of the support) makes the dynamics less affected by the support dynamics (Figure 7.4, left). On the contrary, if a "stiff" nano-hexapod is used, the support dynamics appears in the plant dynamics (Figure 7.4, right).

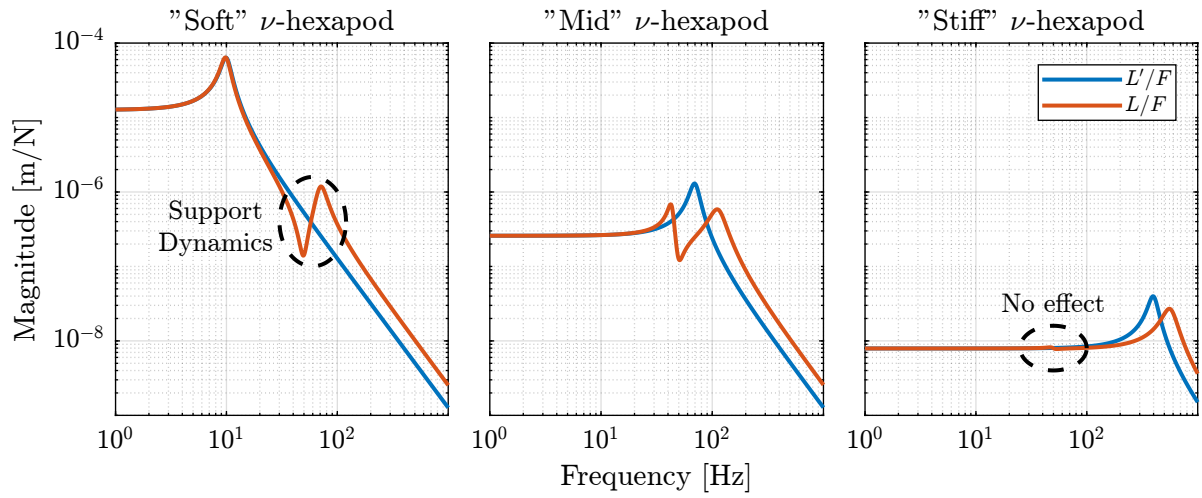


Figure 7.3: Effect of the support compliance on the transfer functions from F to L

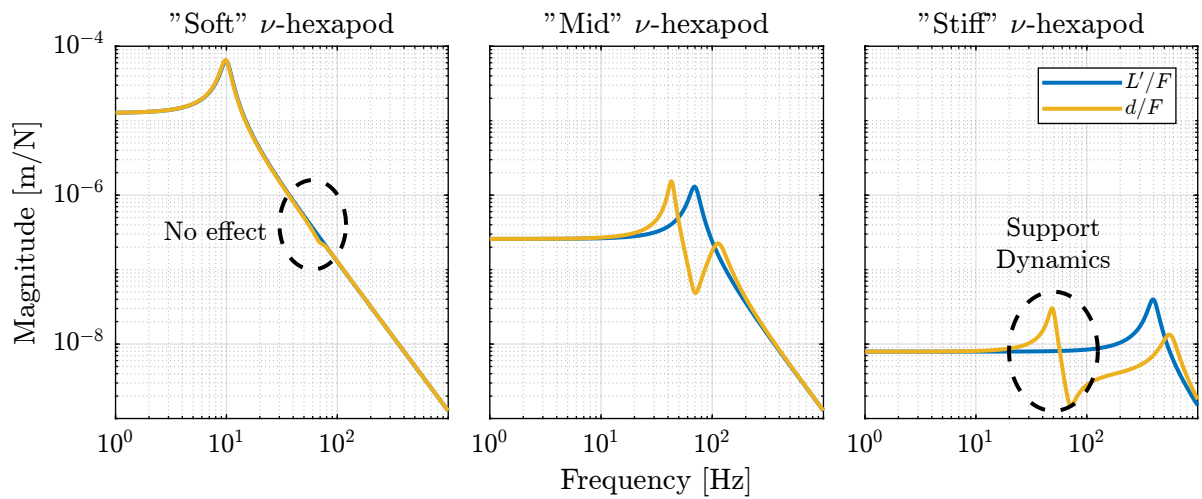


Figure 7.4: Effect of the support compliance on the transfer functions from F to d

Conclusion

Important

In order to study the impact of the support compliance on the plant dynamics, simple models shown in Figure 7.1 were used.

Depending on the quantity to be controlled (L or d in Figure 7.1b) and on the relative location of ω_ν (suspension mode of the nano-hexapod) and ω_μ (modes of the support), the interaction between the support and the nano-hexapod dynamics can change drastically (observations made are summarized in Table 7.1).

For the NASS, having the suspension mode of the nano-hexapod at lower frequencies than the suspension modes of the micro-station would make the plant less dependent on the micro-station dynamics, and therefore easier to control.

Note that observations made in this section are also affected by the ratio between the support mass m' and the nano-hexapod mass m (the effect is more pronounced when the ratio m/m' increases).

Table 7.1: Impact of the support dynamics on the plant dynamics

	$\omega_\nu \ll \omega_\mu$	$\omega_\nu \approx \omega_\mu$	$\omega_\nu \gg \omega_\mu$
d/F :	small	large	large
L/F :	large	large	small

8 Effect of Payload Dynamics

Up to this section, the sample was modelled as a mass rigidly fixed to the nano-hexapod (as shown in Figure 8.1a). However, such sample may present internal dynamics and its fixation to the nano-hexapod may have limited stiffness.

To study the effect of the sample dynamics, models shown in Figure 8.1b are used in this Section.

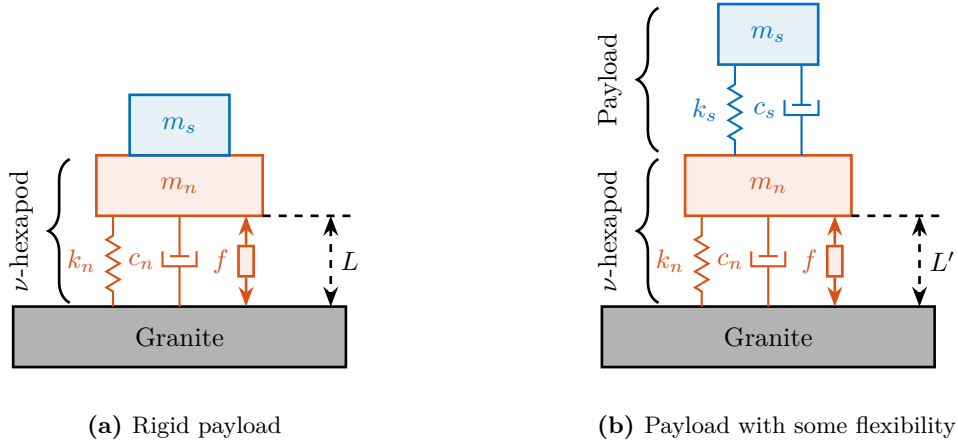


Figure 8.1: Models used to study the effect of payload dynamics

8.1 Impact on the plant dynamics

To study the impact of sample dynamics, the following sample configurations are considered:

- rigid sample, corresponding to Figure 8.1a
- two flexible samples with a resonance at $\omega_s = 200$ Hz and at $\omega_s = 20$ Hz respectively, corresponding to Figure 8.1b
- for all cases, two sample masses are considered: $m_s = 1$ kg and $m_s = 50$ kg

The transfer functions from the nano-hexapod force to the motion of the nano-hexapod top platform are computed for all the above configurations and are compared for a soft Nano-Hexapod $k_n = 0.01$ N/ μ m in Figure 8.2.

It can be seen that the mode of the sample adds an anti-resonance followed by a resonance (zero/pole pattern). The frequency of the anti-resonance corresponds to the “free” resonance of the sample $\omega_s = \sqrt{k_s/m_s}$. The flexibility of the sample also changes the high frequency gain (the mass line is shifted from $\frac{1}{(m_n+m_s)s^2}$ to $\frac{1}{m_n s^2}$).

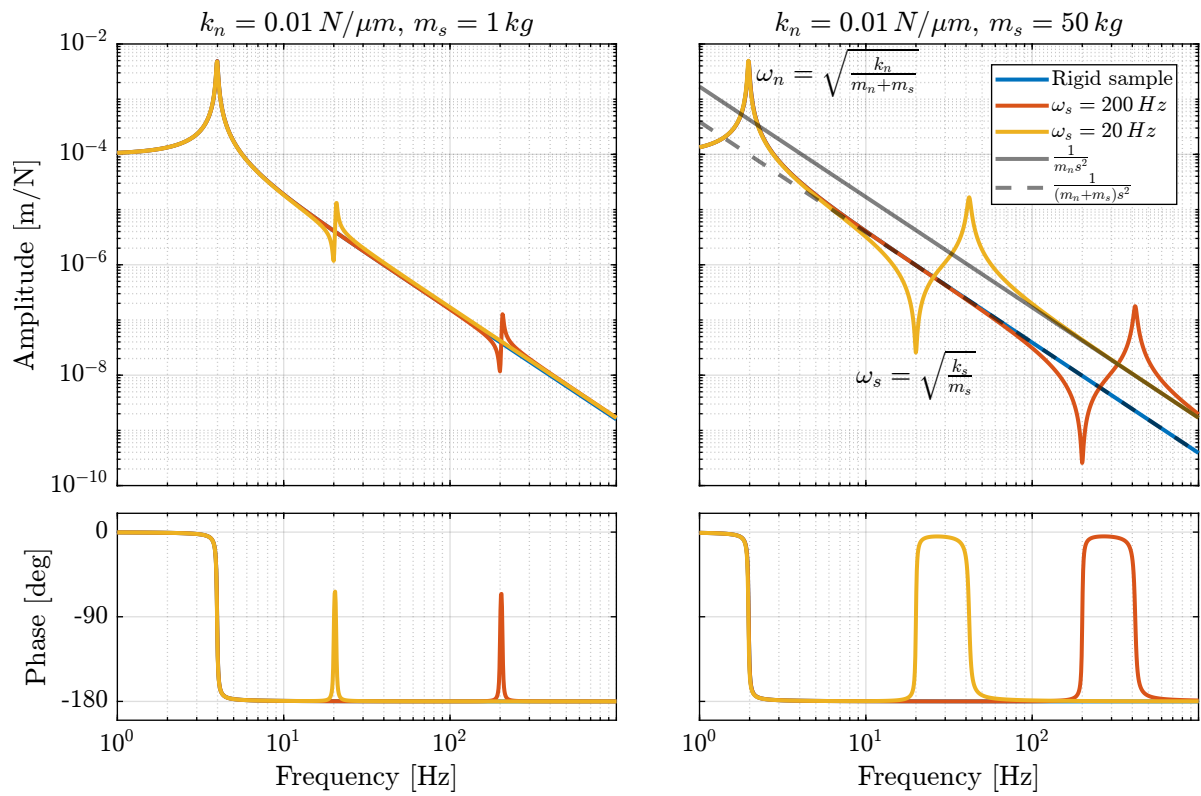


Figure 8.2: Effect of the payload dynamics on the soft Nano-Hexapod. Light sample on the right, and heavy sample on the left

The same transfer functions are now compared when using a stiff nano-hexapod ($k_n = 100 \text{ N}/\mu\text{m}$) in Figure 8.3. In that case, the sample's resonance ω_n is smaller than the nano-hexapod resonance ω_n . This changes the zero/pole pattern to a pole/zero pattern (the frequency of the zero still being equal to ω_s). Even though the added sample's flexibility still changes the high frequency mass line from $\frac{1}{(m_n+m_s)s^2}$ to $\frac{1}{m_n s^2}$, the overall dynamics is much less impacted, even if the sample mass is high (see yellow curve in Figure 8.3, right).

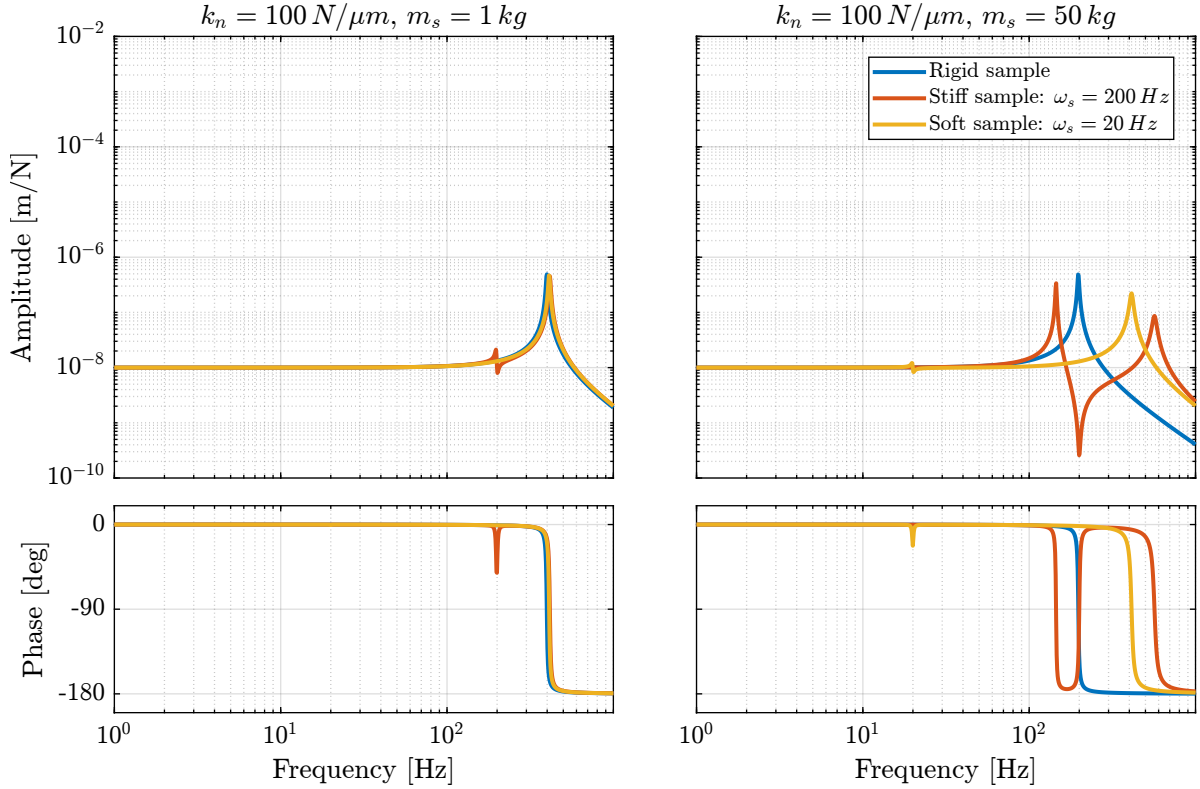


Figure 8.3: Effect of the payload dynamics on the stiff Nano-Hexapod. Light sample on the right, and heavy sample on the left

Important

The impact of the sample dynamics on the plant varies with the sample mass and the relative resonance frequency of the sample ω_s and of the nano-hexapod ω_n . The larger the sample mass, the larger the effect (i.e. change of high frequency gain, appearance of additional resonances and anti-resonances). A zero/pole pattern is observed if $\omega_s > \omega_n$ and a pole/zero pattern if $\omega_s < \omega_n$. Such additional dynamics can induce stability issues depending on their position relative to the wanted feedback bandwidth as explained in [6, Section 4.2].

The general conclusion is that the stiffer the nano-hexapod, the less it is impacted by the payload's dynamics, which would make the feedback controller more robust to a change of payload.

This is why high-bandwidth soft positioning stages are usually restricted to constant and calibrated payloads (CD-player, lithography machines, isolation system for gravitational wave detectors, ...), while stiff positioning systems can more easily accept various payloads.

8.2 Impact on the positioning stability

Having a flexibility between the measured position (i.e. the top platform of the nano-hexapod) and the point-of-interest to be positioned relative to the x-ray can also impact the positioning stability. This is due to the fact that the measured (and therefore controlled) distance is no longer equal to the important distance for the experiment.

In order to estimate if the sample flexibility is critical for the position stability of the point of interest, the model shown in Figure 8.4 is used. This is the same model that was used in Section 6 but with an added flexibility between the nano-hexapod and the sample (considered sample modes are at $\omega_s = 20$ Hz and $\omega_n = 200$ Hz).

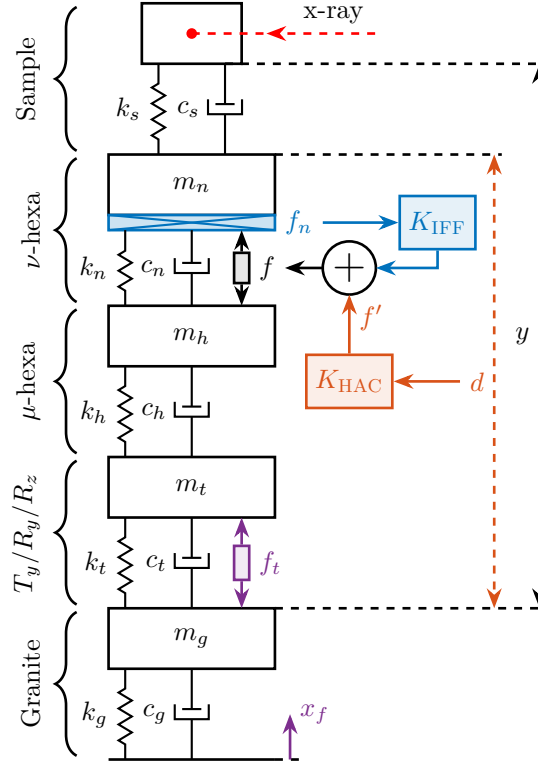


Figure 8.4: Uniaxial model considering a flexibility between the nano-hexapod top platform and the sample. In that case the measured and controlled distance d is different from the distance y that is wish to be controlled

After the system dynamics extracted from the model, IFF is applied using the same gains as the ones used in Section 5. Thanks to the collocation between the nano-hexapod and the force sensor used for IFF, the damped plants are still stable and similar damping values are obtained than when considering a rigid sample.

The High Authority Controllers used in Section 6 are then implemented on the damped plants. The obtained closed-loop systems are stable, indicating good robustness.

Finally, closed-loop noise budgeting is computed for the obtained the closed-loop system and the cumulative amplitude spectrum of d and y are shown in Figure 8.5b. The cumulative amplitude spectrum of the measured distance d (Figure 8.5a) shows that the added flexibility at the sample location have very

little effect on the control performance. However, the cumulative amplitude spectrum of the distance y (Figure 8.5b) shows that the stability of y is degraded when the sample flexibility is considered and is degraded as ω_s is lowered.

What happens is that above ω_s , even though the motion d can be controlled perfectly, the sample's mass is “isolated” from the motion of the nano-hexapod and the control on y is not effective.

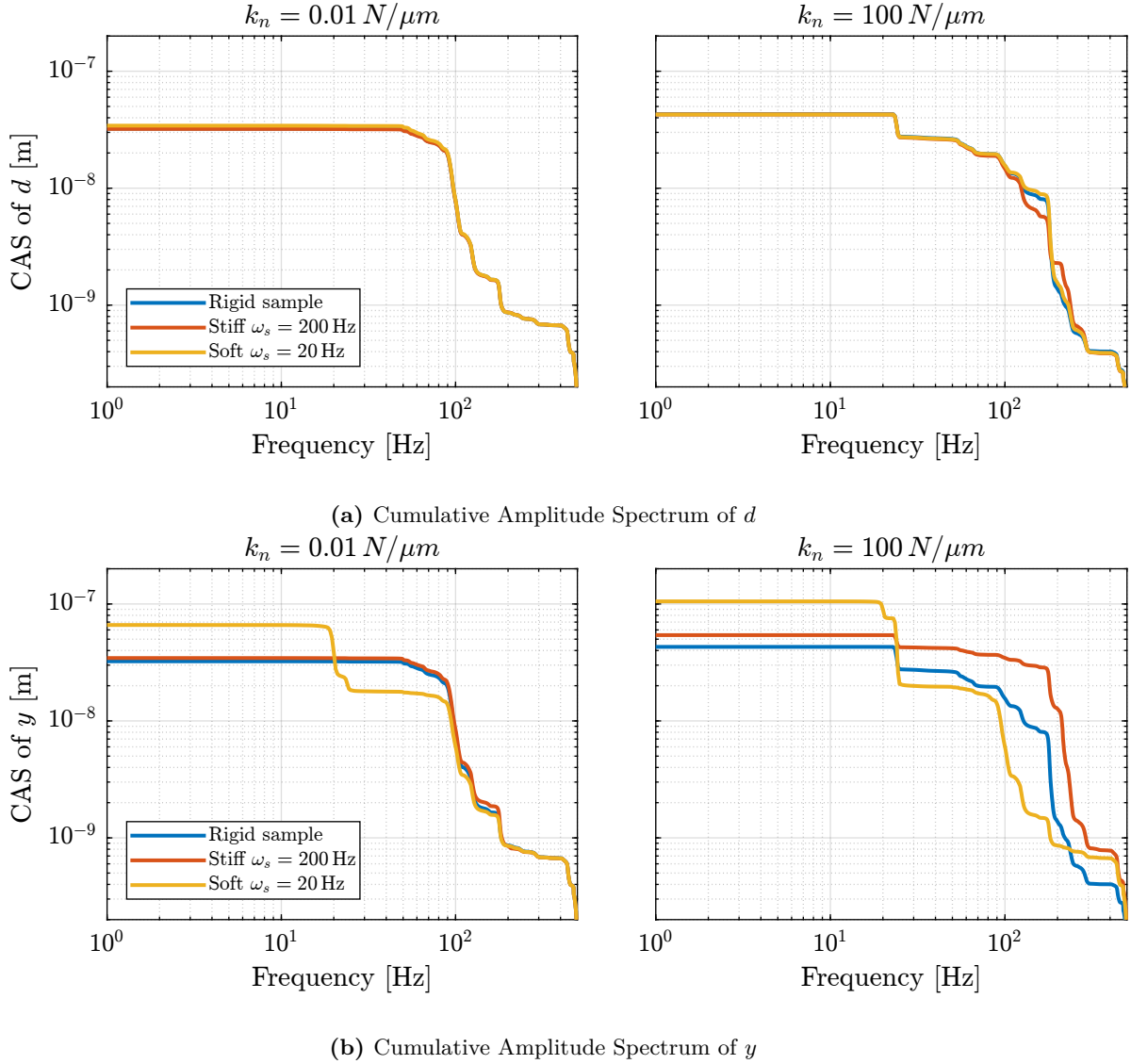


Figure 8.5: Cumulative Amplitude Spectrum of the distances d and y . The effect of the sample's flexibility does not affect much d but is detrimental to the stability of y . A sample mass $m_s = 1$ kg is used for the simulations.

Conclusion

Important

Payload dynamics is usually a major concern when designing a positioning system. For the NASS, the sample may present internal dynamics and limited fixation stiffness to the nano-hexapod platform. On top of that, its mass can vary from 1kg up to 50kg which is a first challenge.

This sample dynamics can add pole/zero or zero/pole pattern in the plant as shown in Section 8.1 which may impact the stability and makes the design of the controller more complex. However, it was shown that this issue is less critical if a stiff nano-hexapod is used.

Having some flexibility between the measurement point and the point of interest (i.e. the sample point to be position on the x-ray) also degrades the position stability as shown in Section 8.2.

It will be therefore important to take special care when designing sampling environments, especially is a soft nano-hexapod is used.

9 Conclusion

In this study, a uniaxial model of the nano-active-stabilization-system has been tuned both from dynamical measurements (Section 1) and from disturbances measurements (Section 3).

It has been shown that three active damping techniques can be used to critically damp the nano-hexapod resonances (Section 5). However, this model does not allow to determine which one is most suited to this application.

Position feedback controllers have been developed for three considered nano-hexapod stiffnesses (Section 6). These controllers were shown to be robust to the change of sample's masses, and to provide good rejection of disturbances. It has been found that having a soft nano-hexapod makes the plant dynamics easier to control (because decoupled from the micro-station dynamics, see Section 7) and requires less position feedback bandwidth to fulfill the requirements. The moderately stiff nano-hexapod ($k_n = 1 \text{ N}/\mu\text{m}$) is requiring a bit more position feedback bandwidth, but it still seems to give acceptable results. However, the stiff nano-hexapod is the most complex to control and gives the worst positioning performance.

Bibliography

- [1] A. Preumont, J.-P. Dufour, and C. Malekian, “Active damping by a local force feedback with piezoelectric actuators,” in *32nd Structures, Structural Dynamics, and Materials Conference*, American Institute of Aeronautics and Astronautics, Apr. 1991 (cit. on p. 19).
- [2] A. Preumont, *Vibration Control of Active Structures - Fourth Edition* (Solid Mechanics and Its Applications). Springer International Publishing, 2018 (cit. on pp. 19, 21).
- [3] D. Karnopp, M. J. Crosby, and R. Harwood, “Vibration control using semi-active force generators,” *Journal of Engineering for Industry*, vol. 96, pp. 619–626, 1974 (cit. on p. 19).
- [4] M. Serrand and S. Elliott, “Multichannel feedback control for the isolation of base-excited vibration,” *Journal of Sound and Vibration*, vol. 234, no. 4, pp. 681–704, 2000 (cit. on p. 19).
- [5] A. Preumont, A. François, F. Bossens, and A. Abu-Hanieh, “Force feedback versus acceleration feedback in active vibration isolation,” *Journal of Sound and Vibration*, vol. 257, no. 4, pp. 605–613, 2002 (cit. on p. 19).
- [6] A. M. Rankers, “Machine dynamics in mechatronic systems: An engineering approach,” Ph.D. dissertation, University of Twente, 1998 (cit. on p. 40).